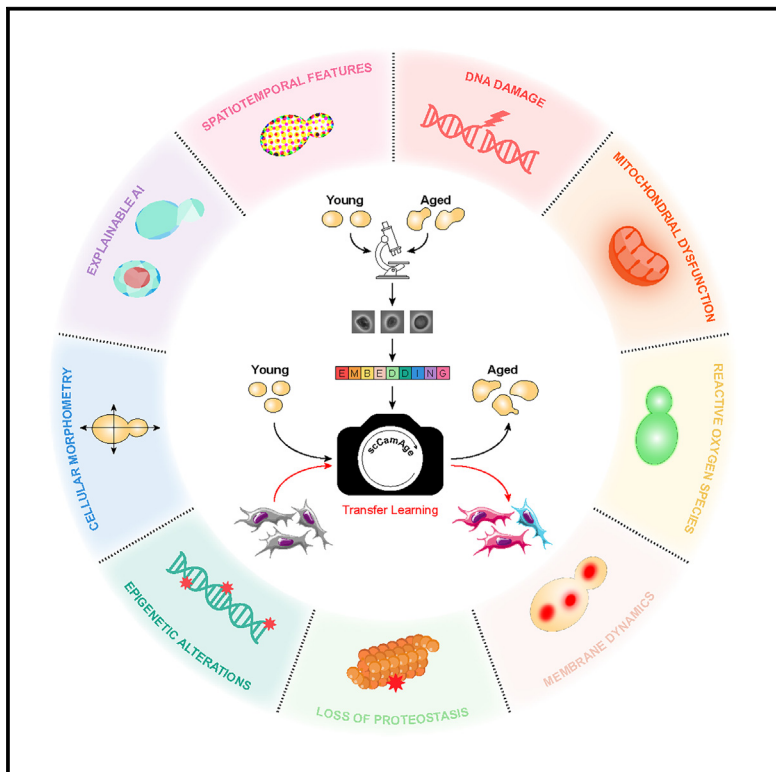


scCamAge: A context-aware prediction engine for cellular age, aging-associated bioactivities, and morphometrics

Graphical abstract



Authors

Vishakha Gautam, Subhadeep Duari, Saveena Solanki, ..., Debarka Sengupta, Anurag Mehta, Gaurav Ahuja

Correspondence

vishakhag@iiitd.ac.in (V.G.), gaurav.ahuja@iiitd.ac.in (G.A.)

In brief

Gautam, Duari et al. developed scCamAge, an AI tool for predicting cell age and age-related bioactivities from micrographs. scCamAge uses the joint representation of image features, cell-shape measurements, and inferred bioactivities. scCamAge was validated for its cross-species applicability and is available as an open-source resource for the community.

Highlights

- scCamAge leverages single-cell image, shape, and bioactivities for age prediction
- scCamAge was rigorously validated using aging-associated drugs and knockouts
- Trained on yeast, scCamAge predicts human fibroblast senescence
- scCamAge unveiled the evolutionary conservation of aging phenotypes



Resource

scCamAge: A context-aware prediction engine for cellular age, aging-associated bioactivities, and morphometrics

Vishakha Gautam,^{1,4,*} Subhadeep Duari,^{1,4} Saveena Solanki,¹ Mudit Gupta,¹ Aayushi Mittal,¹ Sakshi Arora,¹ Anmol Aggarwal,¹ Anmol Kumar Sharma,¹ Sarthak Tyagi,¹ Rathod Kunal Pankajbhai,¹ Arushi Sharma,¹ Sonam Chauhan,¹ Shiva Satija,¹ Suvendu Kumar,¹ Sanjay Kumar Mohanty,¹ Juhi Tayal,³ Nilesh Kumar Dixit,¹ Debarka Sengupta,^{1,2} Anurag Mehta,³ and Gaurav Ahuja^{1,2,5,*}

¹Department of Computational Biology, Indraprastha Institute of Information Technology - Delhi (IIIT-Delhi), Okhla, Phase III, New Delhi 110020, India

²Infosys Centre for AI, Indraprastha Institute of Information Technology - Delhi (IIIT-Delhi), Okhla, Phase III, New Delhi 110020, India

³Rajiv Gandhi Cancer Institute & Research Centre, Sir Chotu Ram Marg, Rohini Institutional Area, Sector 5, Rohini, New Delhi 110085, India

⁴These authors contributed equally

⁵Lead contact

*Correspondence: vishakhag@iiitd.ac.in (V.G.), gaurav.ahuja@iiitd.ac.in (G.A.)

<https://doi.org/10.1016/j.celrep.2025.115270>

SUMMARY

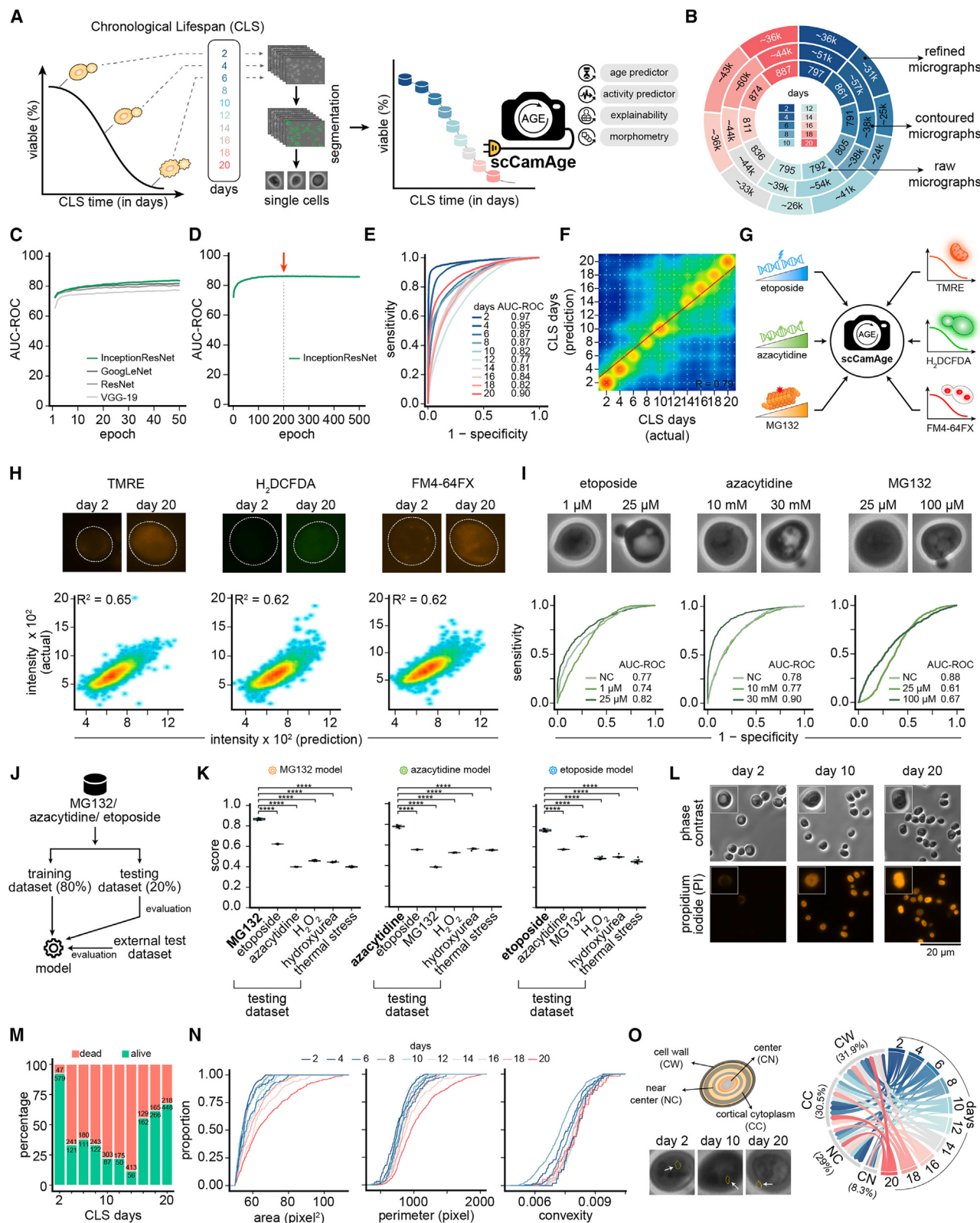
Current deep-learning-based image-analysis solutions exhibit limitations in holistically capturing spatiotemporal cellular changes, particularly during aging. We present scCamAge, an advanced context-aware multimodal prediction engine that co-leverages image-based cellular spatiotemporal features at single-cell resolution alongside cellular morphometrics and aging-associated bioactivities such as genomic instability, mitochondrial dysfunction, vacuolar dynamics, reactive oxygen species levels, and epigenetic and proteasomal dysfunctions. scCamAge employed heterogeneous datasets comprising ~1 million single yeast cells and was validated using pro-longevity drugs, genetic mutants, and stress-induced models. scCamAge also predicted a pro-longevity response in yeast cells under iterative thermal stress, confirmed using integrative omics analyses. Interestingly, scCamAge, trained solely on yeast images, without additional learning, surpasses generic models in predicting chemical and replication-induced senescence in human fibroblasts, indicating evolutionary conservation of aging-related morphometrics. Finally, we enhanced the generalizability of scCamAge by retraining it on human fibroblast senescence datasets, which improved its ability to predict senescent cells.

INTRODUCTION

As cells age, their cellular landscape undergoes dynamic changes in molecular composition, phenotypic expression, and morphological intricacies orchestrated by time.^{1–3} Various methods have been employed to pinpoint cellular age and its associated health, ranging from the traditional, albeit gold-standard methods, such as genetic approaches, to cutting-edge technologies such as deep learning.^{4–6} Recently, single-cell genomics unveiled the aging-associated molecular changes in cells and underpinned its identity, molecular composition, and lineage on the pseudo-temporal scale.^{7–9} Unfortunately, while powerful, it only allows capture of a snapshot of the molecular event and obstructs reassessment along the longitudinal timescale. An alternative standard approach is using conventional genetic lineage-tracing techniques.^{10,11} Despite being powerful, these approaches possess limitations that restrict their implementation and broader utility in aging research.^{12,13} These limitations include stochastic and combinatorial labeling,^{14,15} the

inability to provide high spatial and temporal resolution,¹³ the challenge of capturing fine details of cellular dynamics,¹⁶ and the incorporation of exogenous genetic elements that might restrict native behavior.¹³ Recent investigations have illustrated the capabilities of deep-learning methodologies in self-identifying and self-learning age-associated morphological features by leveraging either facial¹⁷ or cellular microscopic images.¹⁸ For example, studies have demonstrated effective age classification from facial images,¹⁷ introduced the deep learning-based senescence scoring system by morphology (Deep-SeSMo) for identifying senescent cells based on morphological attributes,¹⁹ and showcased the application of deep learning in accurately identifying senescent cells using nuclear morphology or its associated features alone,^{18,20} with subsequent extensions to phenotyping senescent mesenchymal stromal cells.²¹ Despite a surge in deep-learning methods in predicting organismal or cellular age or its associated phenotypes, all the existing solutions lack generalizability, aging-associated bioactivity prediction, and explainability modules that could further support the predictions





(legend on next page)

and facilitate the devising of experimental approaches for downstream mechanism exploration.

Budding yeast *Saccharomyces cerevisiae* serves as an excellent model system for aging research.²² One of the triggering yet unresolved questions is whether the pro- or anti-longevity responses reported in various yeast mutants or upon pharmacological induction are triggered at different or the same chronological time points during aging. Notably, this question is also valid for the mammalian cellular models for aging research, which until now also demanded an array of biochemical and phenotypic assays at different chronological time points, which are both laborious and time consuming. Another fundamental question is whether aging-associated cellular spatiotemporal and morphometric changes are evolutionarily conserved, similar to molecular or pathway-level conservation, despite initial divergent cellular morphologies.²²

To address these and other aforementioned technical complexities, we introduce scCamAge, an advanced transfer learning framework utilizing spatiotemporal data from phase-contrast images for precise single-cell yeast age prediction. scCamAge also includes models for aging-related bioactivity predictions and offers simultaneous calculations of morphometric parameters. scCamAge was rigorously tested on multiple datasets utilizing pro-longevity drugs, genetic loss-of-function mutants harboring distinct longevity patterns, and stress-induced aging responses. We observed a significant increase in replicative lifespan (RLS) in mild thermal stress pulsing (MTSP), which was further validated using integrative high-resolution metabolomics and transcriptomics. Lastly, we tested the

applicability of scCamAge on human datasets for senescence and observed significantly elevated performance, in contrast to the base model, indicating the evolutionary conservation of aging-associated cellular morphometric and bioactivity features. In summary, scCamAge, including the prediction engine, analysis code, and image datasets, is freely available as Docker images and is accessible online at <https://the-ahuja-lab.shinyapps.io/scCamAge/>.

RESULTS

Development of scCamAge prediction engine

Recent advances in deep-learning algorithms for image analysis have significantly enhanced the precision and efficiency of extracting intricate information from microscopic images^{18,19}; however, a comprehensive and adaptable solution, at least in longevity research, is largely missing. Here, we introduce scCamAge, a multi-model, transfer-learning-approach-based solution that facilitates the capture of age-associated phenotypic, biological, and morphometric changes (Figure 1A). To develop scCamAge, we initially generated high-resolution phase-contrast microscopic images of chronologically aging yeast cells, covering ten critical time points from day 2 (young) to day 20 (aged) under optimal growth conditions from three independent large-scale experiments (Figures 1A and S1A; Table S1). We obtained a total of 472,606 single cells, which, upon manual filtering of improperly segmented cells, accounted for 336,514 single cells, representing a loss of ~28.8% of the original number of single cells (Figures 1B, S1B, and S1C).

Figure 1. Development of scCamAge deep-learning architecture

- (A) Schematic diagram presenting the survival curve of yeast chronological aging, emphasizing crucial time points for acquiring micrographs to construct a training dataset for scCamAge modeling. On the right, a diagram outlines the main steps in the scCamAge workflow, including image segmentation to isolate single yeast cells, their utilization in constructing a multi-model for predicting the age of individual yeast cells, and other noted features.
- (B) Donut pie chart displaying the count of raw, contoured, and manually refined single-yeast cell images at specified chronological time points.
- (C) Line plot comparing the performance of generalized transfer learning models InceptionResNet, GoogLeNet, ResNet, and VGG19 on a single-cell yeast chronological aging dataset over 50 epochs.
- (D) Line plot indicating the performance of the transfer learning model InceptionResNet on a single-cell yeast chronological aging dataset over 500 epochs.
- (E) The area under the ROC curve (AUC-ROC) illustrates the one-vs.-all AUC-ROC values under specified conditions.
- (F) Contour scatterplot with overlaid regression line illustrating the correlation between the scCamAge predicted and actual (ground truth) class labels on the held-out dataset of single yeast cells undergoing chronological aging.
- (G) Schematic diagram illustrating aging-associated bioactivities, including cellular reactive oxygen species (ROS) levels, mitochondrial abundance and potential, vacuolar organelle morphology and dynamics, epigenetic modifications, alterations in proteostasis, and genomic instability, along with the strategies employed for their inference.
- (H) Representative micrographic insets depicting the fluorescence of single-cell yeast pre-treated with bioactivity measuring vital dyes. The bottom graphs display the correlation between predicted vs. actual fluorescence intensities in the indicated conditions.
- (I) Representative micrographic insets depicting the phase-contrast single-cell yeast pre-treated with the indicated drugs. The bottom graphs display the AUC-ROC plots for the indicated conditions.
- (J) Schematic representation of the overall strategy used for cross-validation to evaluate the specificity of the indicated drug treatment models.
- (K) Boxplots showing the cross-validation performance results, represented as AUC-ROC values (y axis), for drug-specific models (MG132, azacytidine, and etoposide) evaluated on the specified testing datasets (x axis). The Mann-Whitney U test was used to compute the p values, with a significance threshold of 0.05. *, **, ***, and **** represent p values <0.05, <0.01, <0.001, and <0.0001, respectively.
- (L) Representative micrographs (left) displaying phase-contrast images (top) and corresponding propidium iodide (PI)-stained cells (bottom) at the indicated time points during yeast chronological aging assays. The scale bar represents 20 μ m.
- (M) Barplot (right) shows the relative proportions of live (green) and dead (red) cells quantified at the respective time points.
- (N) Empirical cumulative distribution function (ECDF) plots showing the distributions of cell area, perimeter, and convexity of live yeast cells (PI-negative) at the indicated time points during yeast chronological aging assays.
- (O) Schematic diagram highlighting the key cellular area used for the quantitative analysis of the explainability module of the scCamAge model. Representative micrographs at the bottom depict the scCamAge explainability module guided topmost feature (highlighted in yellow) responsible for chronological age predictions in the indicated conditions. (Right) Circos plot depicting the relative cellular localization of the scCamAge explainability module guided topmost features at critical time points of chronological aging.

Notably, we repurposed the publicly available YeastSpotter model for automated single-cell segmentation²³ (Figure S1D). Furthermore, we used single-cell images instead of whole micrographs to ensure accurate lifespan predictions by eliminating background noise, overlapping cells, and stage variability while capturing critical morphological and phenotypic features. Post image selection, we used a transfer-learning approach and tested four different pre-trained models, i.e., InceptionResNet (vision: v.0.10.0, inception_v3),²⁴ GoogLeNet (vision: v.0.10.0, googlenet),²⁵ ResNet (version 50),²⁶ and VGG 19 (version 19)²⁷ for building the predictor module of scCamAge (Figure S1E). Notably, the InceptionResNet (vision: v.0.10.0, inception_v3) model demonstrated superior performance with the area under the curve (AUC) value, ranging from 72.45 to 83.93 (Figure 1C), and was therefore selected for downstream model reconstruction with hyperparameter optimization (Figures S1F and S1G). The best-performing hyperparameters were applied for 500 training epochs. We observed the highest model performance at the 200th epoch with an AUC of 86.2% and an accuracy of 53.4% (random accuracy is 10%) (Figure 1D). We further evaluated the performance of the model using the stringent area under the receiver-operating characteristic curve (AUC-ROC) comparison, i.e., the one-vs.-all approach, and observed acceptable performances, with AUC values ranging from 0.77 (day 12) to 0.97 (day 2) (Figures 1E and S1H; Table S2). Finally, the model trained at the 200th epoch was selected as the default predictor model and was referred to as the scCamAge model in the further downstream analysis. Additionally, we evaluated the performance of this model in predicting single-cell yeast chronological age using an independent dataset (number of single cells 82,268) and observed a positive correlation (Spearman's correlation value 0.794), indicating the robustness of the scCamAge model (Figure 1F).

Our study demonstrates the capability of scCamAge to predict six critical aging-associated bioactivities, such as reactive oxygen species (ROS) levels, mitochondrial dynamics, vacuolar morphology, epigenetic alterations, proteostasis, and genomic stability (Figure 1G). Leveraging two distinct methodologies, i.e., bioactive dye-based measurements and drug-exposure assays, we systematically captured and analyzed aging signatures from single-cell micrographs. In the first approach, we employed bio-viable fluorescent dyes to directly measure mitochondrial potential, ROS levels, and vacuolar dynamics across ten chronological aging time points in yeast. Single-cell phase-contrast and fluorescent micrographs were taken and paired, and the scCamAge workflow was used to generate embeddings from phase-contrast images. Regression models built using these embeddings achieved strong predictive performance, with R^2 values between 0.62 and 0.65 after rigorous optimization and 10-fold cross-validation (Figures 1G, 1H, S1A, and S2A). Notably, we trained multiple regression models using algorithms such as random forest (RF), XGBoost (XGB), multi-layer perceptron (MLP), RIDGE, and least absolute shrinkage and selection operator (LASSO), and finally selected the RIDGE-based models due to their superior performance (maximum R^2 value) under default settings (Figures S2B and S2C). Notably, to enable scalable screening, we used phase-contrast image embeddings to predict aging-associated bioactivities, as they effectively link im-

age-based features with fluorescent intensities while avoiding the need for co-supplementing fluorescence images during testing.

In the second approach, we exposed cells to non-lethal concentrations of the drugs etoposide, azacytidine, and MG132 to induce DNA damage, epigenetic dysregulation, and proteostasis loss, respectively (Figures 1G, 1I, S1A, and S2A). Classification models trained on scCamAge embeddings and dose information showed robust predictive capability, with AUC values ranging from 0.6 to 0.8 (Figures 1I and S2D–S2F). Notably, we compared the performance of eight different classification-algorithm-based models using these image-specific embeddings (features) along with the treatment dose information (classes) (see STAR Methods). To further rigorously validate the models' performance and to evaluate whether the observed differences are due to generalized stress response or are specific to individual drug treatments, we rebuilt new binary classifiers for each drug (etoposide, azacytidine, and MG132) and validated their performances through rigorous 10-fold cross-validation. Moreover, each drug-specific model was tested by projecting phase-contrast images of their testing data as well as the images from alternative drug-treated yeast cells. Our results demonstrated that while drug-specific models achieved high AUC-ROC values on their respective datasets, projections of alternative datasets yielded AUC-ROC values close to 0.5, suggesting randomized classification. This indicates that the models primarily learned spatiotemporal morphological features specific to each drug rather than generalized stress-related features. Additional experiments incorporating oxidative stress (H_2O_2), thermal stress (42°C), and metabolic stress (hydroxyurea) further supported this finding, as projections of these stress-response datasets also resulted in lower AUC-ROC values (Figures 1J, 1K, S3A, and S3B).

In addition to predicting bioactivities, scCamAge enables automated computation of cellular morphometric features, such as area, perimeter, and convex hull. During yeast chronological aging, morphometric analysis was performed exclusively on viable cells to ensure accuracy. Using chronological lifespan (CLS) assays and propidium iodide (PI) staining, dual-channel imaging allowed the isolation of phase-contrast images for PI-negative (live) cells (Figures 1L, 1M, and S1J). Our analysis revealed a significant age-dependent increase in cellular area, perimeter, and convexity (Figures 1N, S1I, S1K, and S1L). Notably, young cells exhibited greater variance in area and perimeter distributions, which became more uniform with age. This shift was reflected in a leptokurtic kurtosis range of 2.27–2.69, highlighting distinct morphological changes associated with aging. The final component of scCamAge is its explainability module, designed to identify subcellular regions critical for the model's age predictions. Using an external dataset of single-cell images spanning ten chronological aging time points, we observed a dynamic shift in regions of interest. In younger cells (day 2), enrichment was concentrated near the nucleus, while in older cells (day 20) it shifted toward the cell wall (Figure 1O). In summary, scCamAge integrates multiple capabilities: its predictor module offers single-cell resolution age predictions, the bioactivity module predicts six key aging-associated bioactivities, and the explainability and morphometry modules enhance

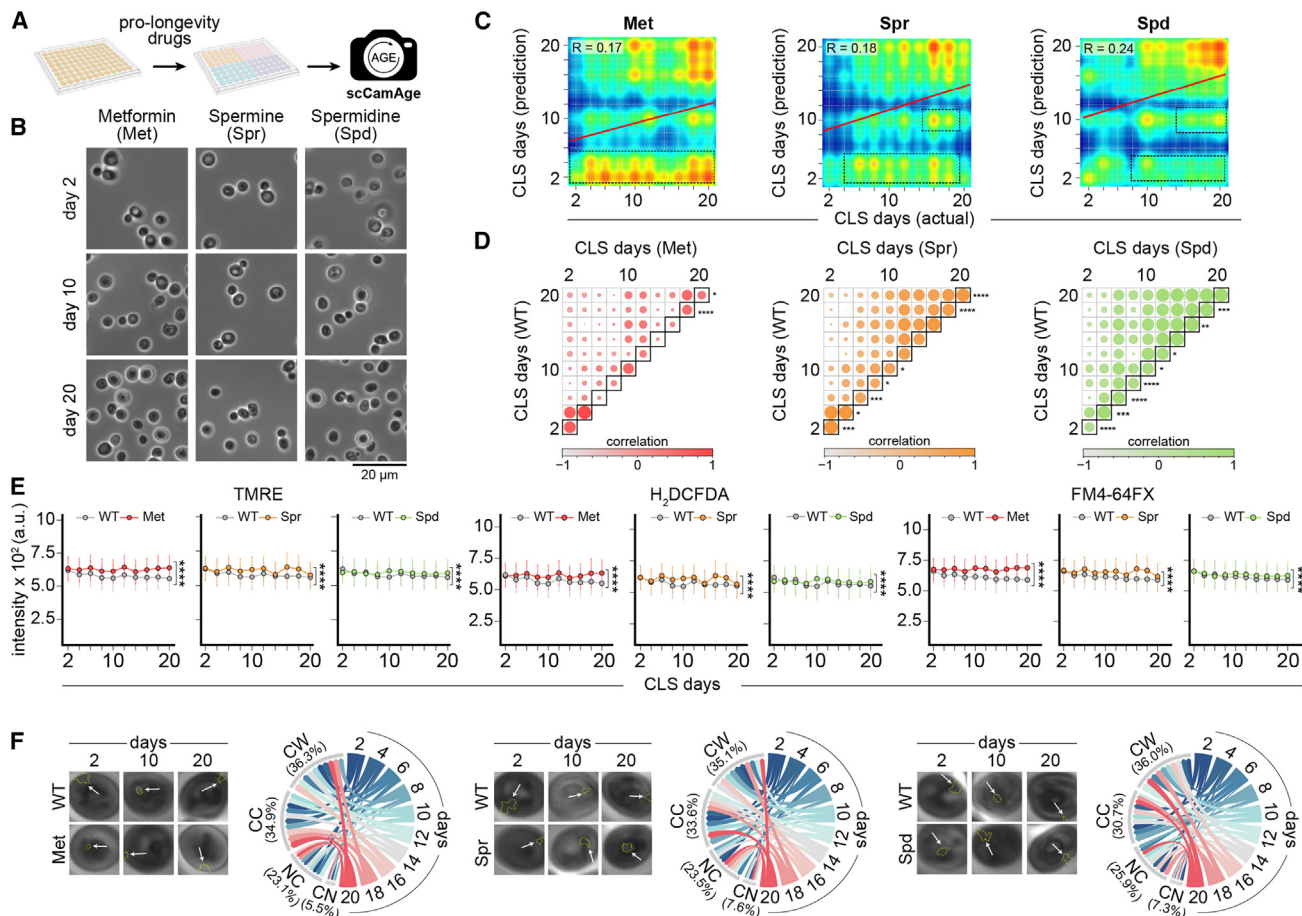


Figure 2. scCamAge reveals longevity effects of pro-longevity drugs using micrograph analysis

- (A) Schematic representation depicting the experimental workflow used to validate scCamAge performance using well-established pro-longevity drugs on chronological lifespan (CLS) assays.
- (B) Representative micrographs showing phase-contrast microscopic images of wild-type (BY4741) yeast cells treated with pro-longevity drugs at specified chronological time points. The scale bar represents 20 μ m.
- (C) Contour scatterplot with overlaid regression line illustrating the correlation between the scCamAge predicted (y axis) and actual (ground truth; x axis) class labels on pro-longevity drug-treated yeast cultures at indicated chronological age time points. Of note, overlaid dotted rectangles represent critical regions responsible for pro-longevity effects.
- (D) Correlation plot depicting pairwise (chronological time points) correlation between untreated and pro-longevity drug-treated conditions. The KS test was performed to compare the distributions of features between the test and control groups. The test provides two key outputs: the D value, which represents the maximum difference between the cumulative distribution functions (CDFs) of the two groups, and the p value, which indicates the statistical significance of the observed difference. A smaller p value (<0.05) signifies a significant difference in the distributions. *, **, ***, and **** indicate p values <0.05 , <0.01 , <0.001 , and <0.0001 , respectively.
- (E) Line plots depicting trends of predicted bioactivities across ten chronological time points for specified conditions. Data represent mean \pm SEM. The p value was calculated using the ANCOVA test, with a significance threshold of 0.05. *, **, ***, and **** correspond to p values <0.05 , <0.01 , <0.001 , and <0.0001 , respectively.
- (F) Representative micrographs depicting the scCamAge explainability module guided topmost feature (highlighted in yellow) responsible for chronological age predictions in specified conditions. Circos plots showing the relative cellular localization of the scCamAge explainability module guided topmost feature at critical time points of chronological aging in the indicated drug-treatment conditions.

interpretability and automate morphometric calculations. Together, these modules establish scCamAge as a comprehensive tool for cellular aging research (Figure 1A).

scCamAge pinpoints temporal longevity activation upon pro-longevity drug treatments

Using scCamAge, we next identified the temporal onset of pro-longevity responses in yeast cells treated with metformin, sper-

mine, and spermidine, known pro-longevity drugs (Figures 2A and 2B). Aliquots were sampled across ten chronological age time points, and phase-contrast micrographs from treated cells (metformin: 20,783 cells; spermine: 23,504 cells; spermidine: 21,827 cells) were analyzed using scCamAge (Figure 2B and Table S1). Our predictions revealed a robust pro-longevity response in metformin-treated cells, evident from a leftward shift on the prediction axis, with onset as early as day 4 of the CLS

assay (Figures 2C and S6A). Spermidine and spermine treatments showed a delayed accumulation of aged cells compared to controls. Pairwise Spearman correlations between chronological time points indicated the strongest longevity response with metformin ($R = 0.17$), followed by spermine ($R = 0.18$) and spermidine ($R = 0.24$) (Figures 2C, 2D, and S6A). These findings align with previously reported pro-longevity effects of these drugs.²⁸

We further explored the impact of metformin, spermine, and spermidine on aging-associated bioactivities by comparing their effects to those in untreated controls. Predictions from dye-based bioactivity analyses revealed elevated mitochondrial potential, ROS levels, and intracellular vacuoles in treated groups (Figures 2E and S4E; Table S8). Notably, while the overall trend is similar across bio-viable dyes, pairwise comparison of the median of the distributions clearly revealed statistical significance at multiple chronological time points. Similarly, by using drug-treatment-based models, we observed a notable reduction in the proportion of cells with elevated DNA damage (class: 25 μ M etoposide) during aging, suggesting these drugs promote genomic stability (Figure S4A). Similarly, fewer cells displayed age-related epigenetic dysregulation across treatments, highlighting their protective effects against epigenetic alterations (classes: 10 mM and 30 mM azacytidine). However, no significant differences were observed in proteostasis loss between treated and untreated cells. Morphometric analysis revealed a significant rightward shift in cellular area and perimeter distributions in metformin-treated cells, indicating an expansion in cell morphology during aging. For spermidine, such shifts were transient and observed only at specific time points (CLS days 6 and 8) (Figure S4B–S4D). Using scCamAge's explainability module, we identified key cellular regions influencing model predictions. Regions of interest (ROIs) were enriched at the cell wall (35%–36%) and cortical cytoplasm (30%–35%) in treated cells, while untreated controls showed higher cytoplasmic enrichment (23%–26%) (Figure 2F). These findings suggest that pro-longevity drugs influence both bioactivity and cellular structure during aging.

scCamAge pinpoints pro- or anti-longevity responses in various yeast knockouts

In yeast aging research, multiple mutants have been characterized for their longevity effect using chronological and RLS assays.^{22,29,30} We next wondered whether the activation of pro-longevity response in the well-characterized loss-of-function mutants is uniform or elicits at different temporal points during chronological aging. To address this, we performed CLS assays on reported pro-longevity mutants and observed varied temporal activation of longevity responses (Figures 3A–3D, S5A–S5C, S6A–S6C, and S7A–S7E). For example, in the case of *pdx3Δ* cells, the onset of pro-longevity response was initiated as early as the chronological age of day 2 or day 4. In contrast, delayed onset was observed in the case of *pho89Δ* and *prs3Δ* cells. Similarly diverse temporal activation of pro-longevity response was observed for *met17Δ*, *met2Δ*, *cys4Δ*, *gre3Δ*, *adh2Δ*, and *ipt1Δ* knockout mutants (Figures S6A–S6C). Notably, these genetic knockouts are reported to possess a 40%–100% average increase in lifespan in the CLS assays in budding yeast (Figure S6B).

Since scCamAge conceptually enables the estimation of both pro- and anti-longevity responses, we also performed similar experiments on well-characterized anti-longevity mutants such as *trx1Δ*, *kgd1Δ*, *sod2Δ*, *alt2Δ*, *gsy2Δ*, and *msw1Δ* and observed comparatively early onset of aging phenotypes (Figures 3C, 3D, S6D, S6E, S6H, and S6I). We next used the bioactivity module of scCamAge and observed elevated mitochondrial potential, ROS levels, and enriched intracellular vacuoles in yeast genetic knockouts (Figures 3E, S5E, S5F, S6F, S6J, and S7F–S7G). In comparing both pro- and anti-longevity knockout yeast cells, we observed dynamic responses in azacytidine-, MG132-, and etoposide-treated conditions across chronological time points, indicating the biological relevance of these well-characterized aging-associated bioactivities in mediating anti- or pro-longevity response (Figures S5D, S6G, and S6K).

Next, we projected single cells from these pro- or anti-longevity yeast knockouts onto the scCamAge explainability module and observed differences in relative enrichment at the cell-wall region based on the top selected feature: pro-longevity mutants (*pho89Δ*, *prs3Δ*, and *pdx3Δ*) showed modulation along chronological time points but ended up with equivalent relative counts on day 2 and day 20, while anti-longevity mutants (*trx1Δ*, *kgd1Δ*, and *sod2Δ*) displayed a more pronounced difference (Figure 3F). The results of the prediction of aging-associated bioactivities further revealed significant differences between the wild-type yeast cells and pro- or anti-longevity knockout cells. All these results reinforce the capabilities of the scCamAge models in tracking yeast cell aging at the single-cell resolution while also enabling the prediction of aging-associated bioactivities.

scCamAge uncovers longevity response in iterative thermally stressed cells

Thermal hormesis refers to exposure to sublethal thermal stress that prompts cells to activate adaptive mechanisms, notably the heat-shock response and upregulation of molecular chaperones, resulting in enhanced stress tolerance phenotype and extended lifespan.³¹ This phenomenon induces longevity response, which is well documented in budding yeast³² to multi-cellular fruit flies³³ and is also validated in human fibroblast-based anti-aging assays.³⁴ We conducted CLS assays to determine whether scCamAge could also detect longevity responses in the yeast cells harboring an episodic thermal stress response (continuous and pulsed). We next explored the impact of thermal pre-conditioning on yeast aging by subjecting cells to continuous optimal temperature (30°C–30°C, steady state [SS]), continuous high temperature (37°C–37°C, heat shock [HS]), and iterative pulsed temperatures (30°C–37°C, thermal pulsed [TP]) (Figures 4A and 4B). All CLS assays were performed at 30°C, regardless of prior treatment conditions. Using the scCamAge workflow, we analyzed over 19,935 (SS), 20,666 (TP), and 25,468 (HS) single cells, revealing distinct aging trajectories across the conditions (Figures 4B, S8B, S8C, S8E, and S8F).

Interestingly, scCamAge predictions indicated a mild pro-longevity response under TP conditions, contrasting with an anti-longevity response observed for HS-treated cells (Figure 4D). The explainability module highlighted a striking shift in the enrichment of key features from the nuclear region to the

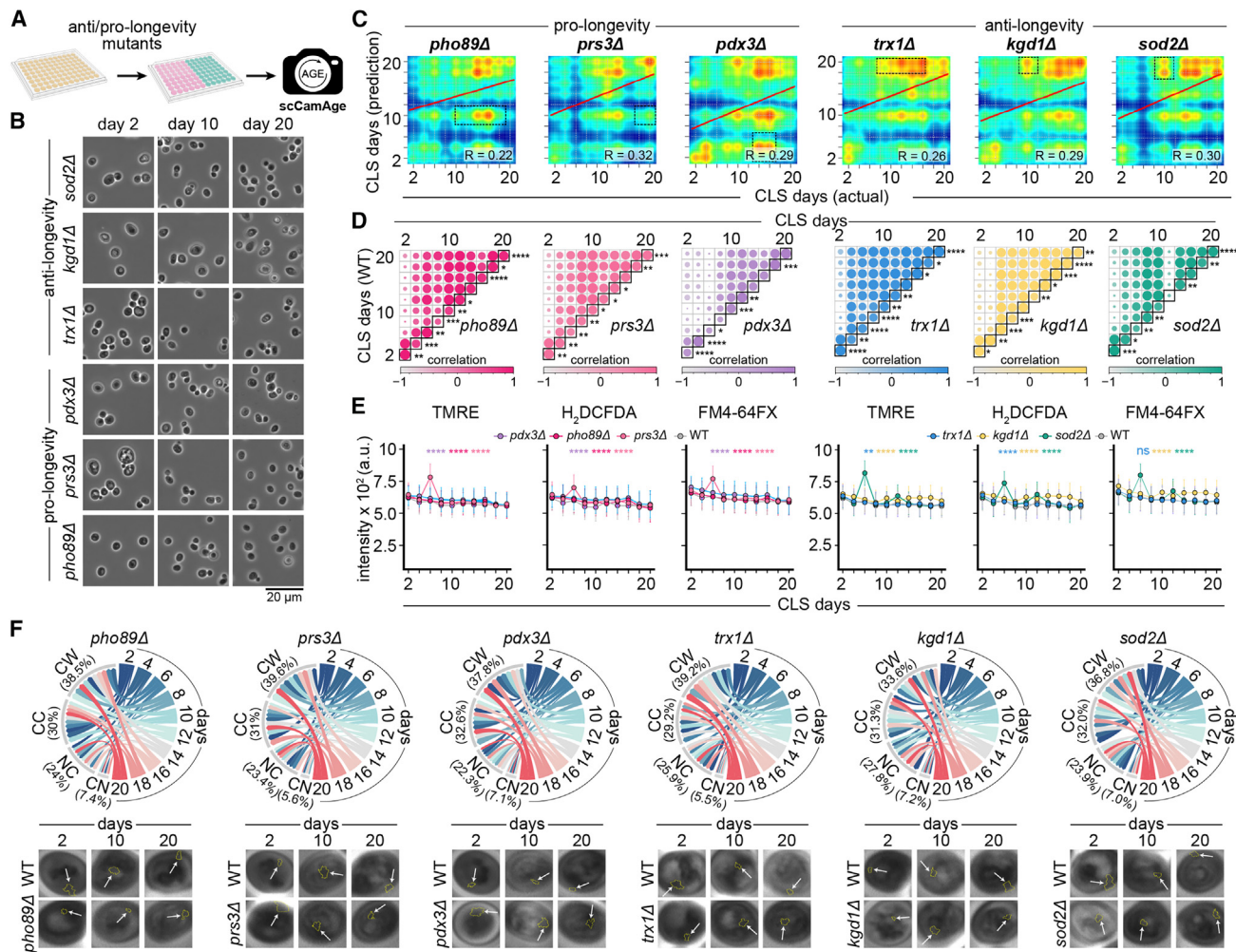


Figure 3. scCamAge tracks pro- or anti-longevity responses in yeast knockouts

- (A) Schematic representation illustrating the experimental workflow used to validate scCamAge performance using well-established pro- and anti-longevity genetic yeast knockouts.
- (B) Representative micrographs displaying phase-contrast microscopic images of indicated genetic knockout yeast cells harboring pro- or anti-longevity effects in CLS assays. The scale bar represents 20 μ m.
- (C) Contour scatterplot with overlaid regression line illustrating the correlation between the scCamAge predicted and actual (ground truth) chronological time points in CLS assays of specified pro- or anti-longevity genetic knockouts.
- (D) Correlation plot depicting pairwise (chronological time points) correlation between wild-type and indicated genetic mutants with reported pro- or anti-longevity phenotypes in yeast CLS assays. The KS test was performed to compare the distributions of features between the test and control groups. The test provides two key outputs: the D value, which represents the maximum difference between the cumulative distribution functions (CDFs) of the two groups, and the p value, which indicates the statistical significance of the observed difference. A smaller p value (<0.05) signifies a significant difference in the distributions. *, **, ***, and **** represent p values <0.05 , <0.01 , <0.001 , and <0.0001 , respectively.
- (E) Line plots depicting trends of predicted bioactivities across ten chronological time points for specified conditions. Data represent mean \pm SEM. The p value was calculated using the ANCOVA test, with a significance threshold of 0.05. *, **, ***, and **** represent p values <0.05 , <0.01 , <0.001 , and <0.0001 , respectively.
- (F) Representative micrographs depicting the scCamAge explainability module guided topmost feature (highlighted in yellow) responsible for chronological age predictions in specified conditions. Circos plots showing the relative cellular localization of the scCamAge explainability module guided topmost feature at critical time points of chronological aging.

cell wall under TP, an effect not observed in SS or HS conditions (Figure 4D). This pattern mirrored explainability results from pro-longevity drug treatments (Figure 2F). Further bioactivity assessments showed dynamic changes in fluorescence intensity under TP, with an initial decrease followed by resurgence during later aging stages (Figures S8D and S8G). Conversely, HS conditions

demonstrated the opposite trend, and SS displayed mixed responses (Figures 4C and S8A). However, experimental CLS assays did not reveal statistically significant differences between SS and TP groups, suggesting that the observed pro-longevity predictions might be more relevant to RLS due to adequate evidence in the literature (Figures 4E–4G). To evaluate this, we

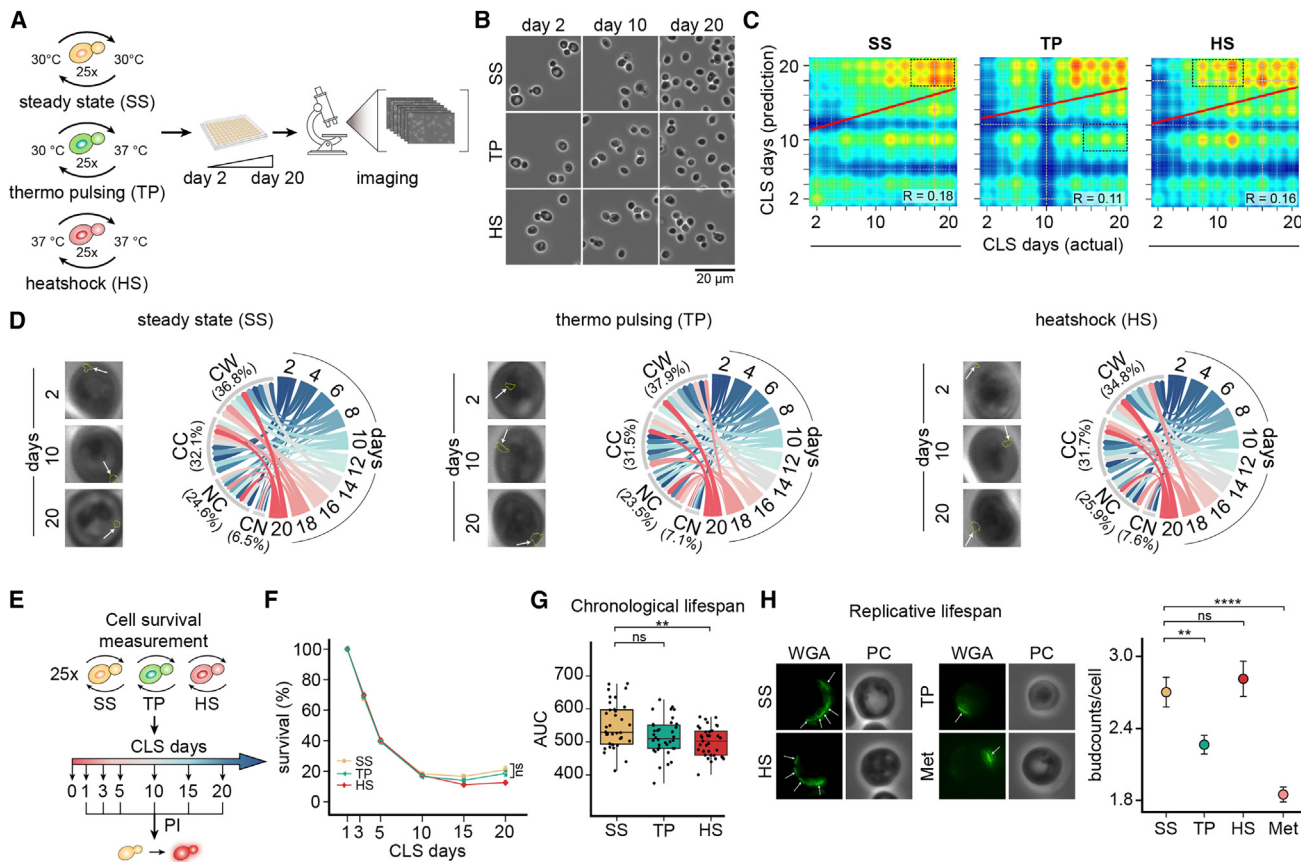


Figure 4. scCamAge unveils impact of iterative thermal stress on yeast replicative lifespan

(A) Schematic representation detailing the methodological approach used to prime yeast cell cultures with iterative thermal stress responses. Thermal pulsing (TP) involves thermal pulsing for 15 min each at 30°C and 37°C for 25 cycles. Steady-state (SS) and heat-shock (HS) conditions entail similar pulsing at 30°C and 37°C, respectively, for the same number of cycles.

(B) Representative micrographs displaying phase-contrast microscopic images of thermal pulsed (TP), steady-state (SS), and heat-shock (HS) yeast cells at specified chronological age time points. The scale bar represents 20 μ m.

(C) Contour scatterplot with overlaid regression line illustrating the correlation between scCamAge predicted and actual (ground truth) class labels in the indicated conditions.

(D) Representative micrographs displaying the top feature (highlighted in yellow) identified by the scCamAge explainability module, responsible for predicting chronological age under specified conditions. Circos plots illustrate the relative cellular localization of this top feature at critical time points during chronological aging in the indicated conditions.

(E) Schematic representation illustrating key time points in the CLS assay used to test the scCamAge model under specified conditions: thermal pulsed (TP), steady-state (SS), and heat-shock (HS).

(F) Survival plot depicting results of CLS assay on wild-type yeast cells under specified conditions: thermal pulsed (TP), steady-state (SS), and heat-shock (HS). The p value was computed using the Mann-Whitney U test (default cutoff 0.05). ns, *, **, ***, and **** refer to p values non-significant, <0.05 , <0.01 , <0.001 , and <0.0001 , respectively.

(G) Boxplot quantifying the area under the survival curve from the CLS assays under indicated conditions. The p value was computed using the Mann-Whitney U test (default cutoff 0.05). *, **, ***, and **** refer to p values <0.05 , <0.01 , <0.001 , and <0.0001 , respectively.

(H) Representative micrographs displaying wheat germ agglutinin staining marking bud scars on the cell wall of single yeast cells (marked with arrowheads) in indicated conditions. The mean-whisker plot on the right quantifies the number of bud counts per cell in indicated conditions. Data represent mean \pm SEM. The p value was calculated using the Mann-Whitney U test, with a default significance threshold of 0.05. *, **, ***, and **** denote p values <0.05 , <0.01 , <0.001 , and <0.0001 , respectively.

performed RLS assays by quantifying the number of buds using wheat germ agglutinin (WGA) staining,³⁵ using metformin-treated cells as a positive control.^{22,36} Quantitative results showed significantly fewer buds in TP and metformin-treated cells compared to SS or HS groups, indicating a reduced replicative aging response (Figure 4H). This aligns with scCamAge pre-

dictions, suggesting that the anti-aging effects in TP are linked to bud-related morphometric features at the cell wall.

Integrative omics validates scCamAge predictions

To elucidate regulators of RLS extension in iterative thermally stressed yeast cells (TP), we conducted transcriptomic analyses.

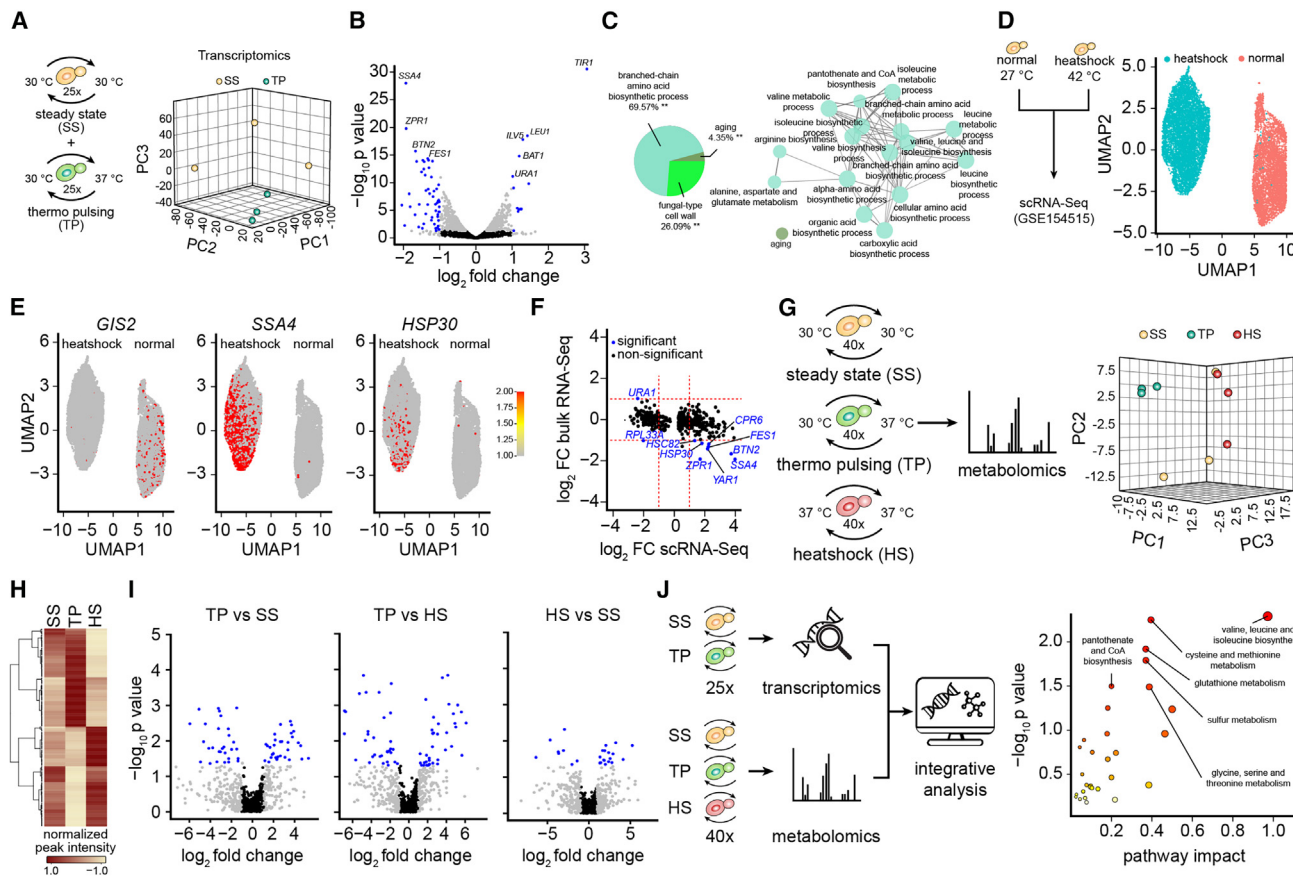
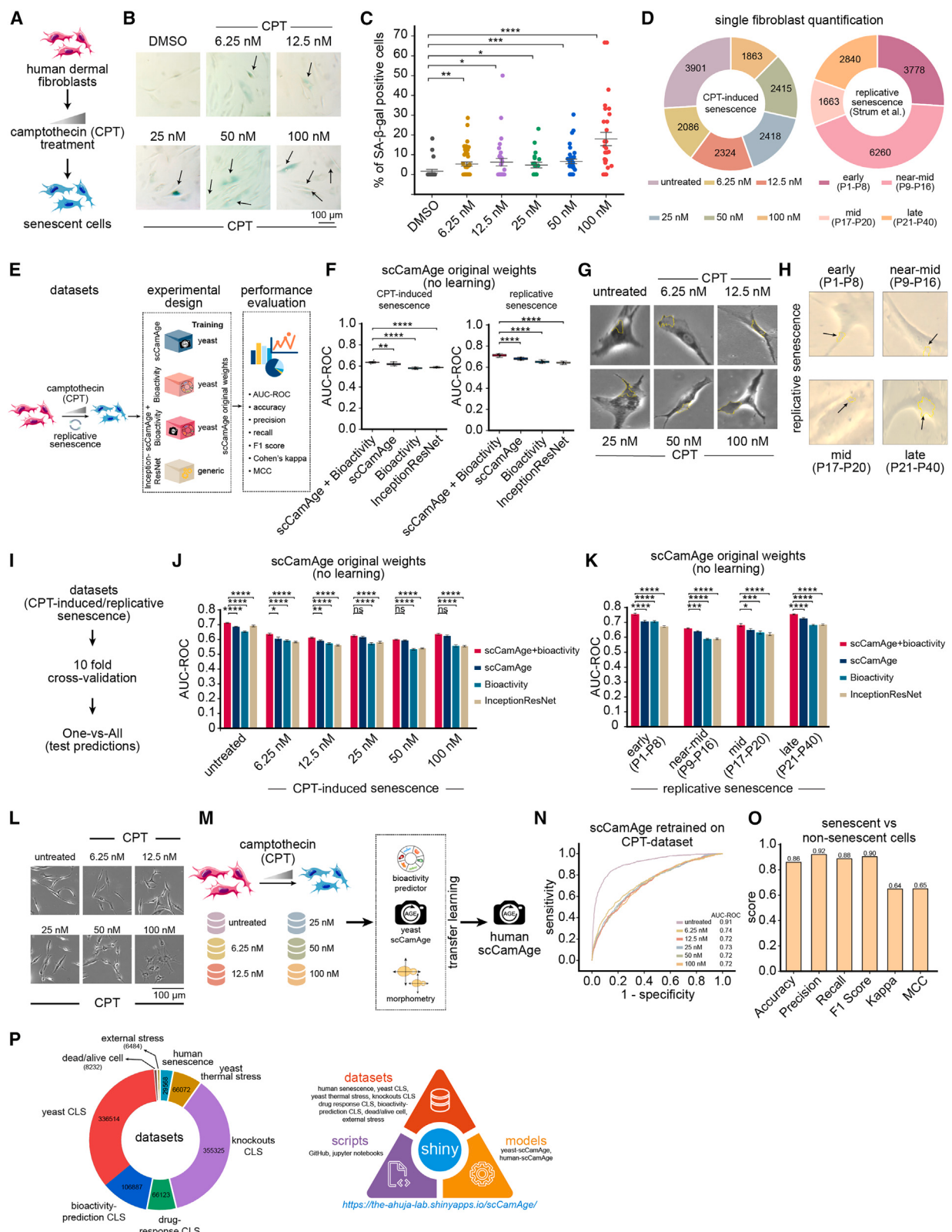


Figure 5. Integrative analysis identifies regulators of yeast replicative lifespan under iterative thermal stress

- (A) Schematic diagram depicting the experimental scheme for preparing transcriptomics samples. Principal-component analysis (PCA) depicting individual sample replicates segregated in a low-dimensional space based on their transcriptomics profiles.
- (B) Volcano plot depicting differentially expressed genes identified between thermal pulsed (TP) and steady-state (SS) conditions.
- (C) Pie chart depicting relative enrichment of prominent gene ontologies identified from differentially expressed genes between thermal pulsed (TP) and steady-state (SS) conditions. The network on the right depicts key functional nodes prominently representing differentially expressed genes.
- (D) Schematic representation detailing experimental conditions used in single-cell transcriptome analysis. (Right) Uniform manifold approximation and projection (UMAP) representations of single-cell transcriptome profiles of indicated conditions.
- (E) Scatterplot highlighting expression of *G/S2*, *SSA4*, and *HSP30* in low-dimensional UMAP space.
- (F) Scatterplot depicting relative enrichment and de-enrichment of differentially expressed genes between statically stressed single-cell yeast transcriptome and thermo-pulsed bulk transcriptomes of yeast cells.
- (G) Schematic representation detailing experimental conditions used in preparing metabolomics samples. PCA on the right depicts individual sample replicates segregated in a low-dimensional space based on their metabolic profiles.
- (H) Heatmap depicting differentially (de)-enriched metabolites in indicated conditions.
- (I) Volcano plots depicting differentially enriched/de-enriched metabolites in indicated conditions.
- (J) Schematic diagram detailing integrative analysis involving transcriptomes and metabolomics profiles. The scatterplot on the right depicts key metabolic pathways differentially enriched upon thermal pulsing. The *p* value was computed using the Fisher's exact test (default cutoff 0.05).

Yeast cells were exposed to either optimal (30°C–30°C, SS) or pulsed (30°C–37°C, TP) thermal stress for 25 cycles (15 min each) (Figure 5A). Post stimulation, RNA sequencing (RNA-seq) was performed, and principal-component analysis (PCA) revealed clear segregation between TP and SS samples across three components (PC1, PC2, and PC3) (Figures 5A and S9A–S9E). Differential gene-expression analysis identified several key transcripts, including *URA1*, *LEU1*, and *ILV5*, known for their association with pro-longevity responses in yeast and other models (Figure 5B and Table S3) (<https://genomics.senescence.info/genes>).^{30,37} Gene ontology analysis highlighted

prominent pathways such as amino acid biosynthesis, fungal cell wall remodeling, and aging, corroborating the predictions of scCamAge and experimental RLS assay results (Figures 5C and S9F). To further investigate transcriptional adaptation, we reanalyzed a public single-cell RNA-seq dataset, comparing cells under continuous thermal stress (42°C) to those under normal conditions (27°C) (Figure 5D). Standard analyses revealed two distinct clusters corresponding to the conditions. Known upregulated HS-induced genes (e.g., *HSP26*, *HSP42*, *SSA4*, *HSP12*, *BTN2*, *HSP78*) and downregulated genes (e.g., *TIF3*, *RPL43A*, *SSB1*, *TRX2*, *IMH1*) were consistent with



(legend on next page)

expected thermal stress responses. Interestingly, we identified a subset of genes (e.g., *SSA4*, *BTN2*, *FES1*) that exhibited reversed expression patterns under mild thermal stress pulsing (TP) compared to continuous thermal stress, suggesting an adaptive transcriptional mechanism (Figures 5E and 5F). These findings highlight unique transcriptional signatures associated with TP, further supporting its mild pro-longevity effects.

To further investigate the metabolic basis of pro-longevity phenotypes in TP yeast cells, we conducted high-resolution untargeted metabolomics (Figures 5G–5I, S9G, and S9H; Tables S4 and S5). The analysis revealed the activation of multiple metabolic pathways previously implicated in lifespan regulation. Notably, pyrimidine metabolism and vitamin B6 metabolism were significantly enriched in TP compared to SS or HS conditions, underscoring their potential roles in lifespan modulation (Figures S9I and S9J). To gain a comprehensive understanding, we performed integrative omics analysis by combining transcriptomic and metabolomic datasets. This approach identified key metabolic pathways, including valine, leucine, and isoleucine biosynthesis, glutathione metabolism, and cysteine and methionine metabolism, as critical regulators of the pro-longevity phenotypes observed in mild thermal stress pulsed (MTSP) or TP yeast cells (Figures 5J and S10A–S10C; Table S6). These findings corroborate the predictions made by the scCamAge workflow and unveil potential regulatory genes and pathways mediating the longevity response under TP conditions.

scCamAge unveiled evolutionary conservation of aging-related morphometrics and bioactivities

Aging-associated cellular pathways^{22,29,38} and morphometric changes, such as cellular enlargement,³⁹ altered mitochondrial morphology,⁴⁰ and reduced nucleolar size,⁴¹ are evolutionarily

conserved from yeast to humans. Leveraging these conserved features, we hypothesized that the scCamAge model, trained on yeast chronological aging datasets, could effectively classify senescent cells in human cell cultures. To test this, we generated a camptothecin (CPT)-induced senescence dataset using primary human fibroblasts treated with varying CPT concentrations (Figures 6A–6D). Quantification of senescence-associated β -galactosidase (SA- β gal) staining confirmed increased senescent cell populations at higher CPT doses. Phase-contrast microscopy images of unstained fibroblasts were then segmented to isolate single cells and categorized based on CPT exposure (Figure 6C). Remarkably, without additional training or adaptation, the yeast-trained scCamAge model successfully identified and classified senescent fibroblasts in these datasets, demonstrating its capability to generalize across species and aging contexts using conserved morphometric hallmarks (Figures 6E and 6F). Notably, the scCamAge model was built on the InceptionResNet architecture using a transfer-learning approach, and when applied without additional training scCamAge significantly outperformed the base InceptionResNet model, validating the evolutionary conservation of these morphometric features (Figures 6F–6J and S11A–S11D). Moreover, the integration of bioactivity features further enhanced classification accuracy, highlighting the evolutionary conservation of aging-associated bioactivities (Figure 6G). Finally, to further evaluate these findings, we tested scCamAge on an independent replicative senescence dataset from Sturm et al. (Figures 6D and 6H).⁴² Without additional learning or weight reassignment, scCamAge once again outperformed the base InceptionResNet model. The integrated embeddings (scCamAge plus bioactivities) provided the most accurate predictions (Figures 6F–6H, 6K, S11A, and S11E–S11G). Overall, these

Figure 6. scCamAge reveals evolutionary conservation of aging-mediated cellular morphological changes

- (A) Schematic diagram depicting the key steps used for camptothecin (CPT)-induced senescence in primary human fibroblasts.
- (B) Representative micrographs depicting camptothecin (CPT)-induced senescent cells marked using senescence associated β -galactosidase assay (SA- β gal assay) staining on primary human fibroblasts. Different concentrations of camptothecin were used, and dimethylsulfoxide (DMSO) served as a solvent control. The scale bar represents 100 μ m.
- (C) Mean whisker plot depicted the percentage of SA- β -gal positively stained cells per image in indicated conditions. Data represent mean \pm SEM. Asterisks indicate statistical significance based on the Wilcoxon rank-sum test, with a p-value cutoff of 0.05, where *, **, ***, and **** correspond to p values <0.05, <0.01, <0.001, and <0.0001, respectively.
- (D) Donut pie chart representing the number of single-fibroblast cell images in CPT-induced and replicative senescence datasets in the indicated conditions.
- (E) Schematic diagram depicting the analysis workflow used to compare the performance of scCamAge, aging-associated bioactivities alone, scCamAge plus bioactivities, and generic InceptionResNet on the CPT-induced senescence dataset or replicative senescence dataset.
- (F) Boxplot depicting the AUC of the testing CPT-induced senescence dataset and replicative senescence dataset. Asterisks denote statistical significance using the Wilcoxon rank-sum test. The p value cutoff used is 0.05. *, **, ***, and **** refer to p values <0.05, <0.01, <0.001, and <0.0001, respectively.
- (G) Representative micrographs showcasing the top feature (highlighted in yellow) identified by the scCamAge explainability module for CPT-induced senescence.
- (H) Representative micrographs showcasing the top feature (highlighted in yellow) identified by the scCamAge explainability module in the replicative senescence dataset.
- (I) Workflow representing the method used to calculate the AUC scores using the one-vs.-all method.
- (J) Barplots depicting the AUC-ROC values across each class of CPT-induced senescence. Data represent mean \pm SEM. The p value was computed using the Mann-Whitney U test (default cutoff 0.05). *, **, ***, and **** refer to p values <0.05, <0.01, <0.001, and <0.0001, respectively.
- (K) Barplots depicting the AUC-ROC values across each class of replicative senescence. Data represent mean \pm SEM. The p value was calculated using the Mann-Whitney U test with a default significance cutoff of 0.05, where *, **, ***, and **** represent p values <0.05, <0.01, <0.001, and <0.0001, respectively.
- (L) Representative micrographs depicting camptothecin (CPT)-induced senescent cells at indicated concentrations. The scale bar represents 100 μ m.
- (M) Schematic diagram depicting the analysis workflow used to create human scCamAge in which yeast scCamAge alongside bioactivity and morphometry predictions were used.
- (N) The area under the ROC curve (AUC-ROC) illustrates the one-vs.-all AUC-ROC values under specified conditions.
- (O) Barplot depicting various evaluation parameters showing prediction power of human scCamAge.
- (P) Schematic diagram representing the offerings of the scCamAge resources.

results suggest that despite a billion years of evolutionary divergence between yeast and human fibroblasts, aging-induced cellular phenotypes, their morphometric markers, and associated bioactivities remain highly conserved.

Enhancing scCamAge generalizability with human fibroblast senescence models

To expand the capabilities of scCamAge, we adapted its yeast-specific predictive models to applications in human senescence using a transfer-learning approach (Figure 6L). The yeast-trained scCamAge model was further trained on the CPT-induced senescence dataset of human fibroblasts and demonstrated a much higher capability to identify senescence features in human cells (Figure 6L). For this adaptation, we utilized phase-contrast micrographs captured across five CPT concentrations previously validated for senescence induction using SA- β -gal staining. Transfer learning was employed, leveraging scCamAge's base model alongside its bioactivity and morphometry modules and training on the CPT-induced human fibroblast senescence dataset. The model achieved peak performance at the 135th epoch out of 500, attaining a one-vs.-all AUC of 0.72–0.91, an accuracy of 52.4% in multi-class classification (random accuracy = 16.7%), and ~86% accuracy in binary classification of senescent vs. non-senescent cells. Precision and recall scores for binary classification were ~92% and ~88%, respectively (Figures 6M–6O). These results validate scCamAge's ability to generalize across species, making it a robust tool for senescence detection in human cells.

To support broader research, we developed a dedicated resource comprising single-cell image datasets from yeast (chronological aging, bioactivity predictions, and thermal stress) and human fibroblasts (CPT- and replication-induced senescence). This resource, along with hyperparameter-tuned models (yeast scCamAge, scCamAge with bioactivity and morphometry, and human-specific scCamAge models), is available as Docker images and Jupyter notebooks for reproducibility and benchmarking (Figure 6P). In summary, our comprehensive resource, featuring diverse single-cell image datasets and hyperparameter-tuned models, will serve as a crucial toolkit for advancing research on cellular aging and senescence.

DISCUSSION

Despite the genomic divergence noted across various species and the accompanying diversity in their aging-related mechanisms, it is striking that the molecular processes underlying aging display a pronounced conservation between *Saccharomyces cerevisiae* and humans.^{22,29} This conservation is particularly notable considering ~1 billion years of evolutionary divergence between these taxa. Among the widely adopted eukaryotic model systems utilized for aging research and for assessing anti-aging interventions, budding yeast is distinguished by its relatively short lifespan and suitability for high-throughput screenings. This widespread adoption can be attributed to its amenability to genetic manipulation and chemical perturbations and its utility in large-scale experimental setups.^{22,28,43,44} Notably, several anti-aging compounds currently undergoing clinical trials, including spermidine, rapamycin, resveratrol, and

metformin, have also demonstrated potent anti-aging effects in yeast.²² This evidence not only underscores the shared aging pathways between yeast and humans but also highlights the effectiveness of yeast as an experimental model for identifying and testing potential anti-aging therapeutics. Other striking evidence includes the aging-associated induction of molecular events documented as hallmarks of human aging.³ Some of the aging phenotypical markers that are shared among humans and yeast include aging-associated ROS accumulation, increase in damaged organelles and proteins, loss of genomic stability and plasma membrane integrity, telomeric alterations, and induction of apoptosis/programmed cell death, among others.^{45,46} All these points clearly reinforce the importance and relevance of budding yeast in initial large-scale screening to narrow down potential chemical anti-aging.

In this study, we introduce scCamAge, a context-aware, transfer-learning-based prediction engine designed for the image-based prediction of chronological age, estimating aging-related bioactivities, and identifying morphometric changes. scCamAge also illuminates the cellular regions crucial to chronological age predictions, offering insights into aging mechanisms through explainable AI (XAI). This innovative methodology overcomes current limitations by offering a more comprehensive understanding of aging. One of the key strengths of scCamAge is its ability to capture the complex interactions among aging-related processes, including genomic instability,^{47,48} the production of ROS,⁴⁹ and mitochondrial content and dynamics.⁵⁰ While previous deep-learning-based solutions have demonstrated remarkable performance in detecting senescent cells both in culture and in tissue sections, to the best of our knowledge, none have provided predictions of bioactivities directly from micrographs.^{18,19} This additional feature serves as an initial proof of principle for future frameworks to develop image-based predictive models by co-leveraging bioactivities. While focused on the aging process, this approach could potentially extend to other scientific fields as well.

We rigorously tested scCamAge by validating on held-out and independent datasets and using datasets of pro-longevity drug treatments and genetic knockouts.^{28,30} All these experiments confirm the accuracy and reliability of scCamAge in predicting cellular age and capturing aging-related changes. Furthermore, scCamAge's ability to reveal significant molecular alterations and anti-aging responses in yeast cells subjected to thermal stimuli underscores its utility in studying dynamic cellular processes. While the scCamAge model is built on yeast datasets, its capability to successfully predict human fibroblast senescence (chemical- or replication-induced senescence) highlights its cross-species applicability and the evolutionary conservation of aging-associated morphometric changes.⁴⁵ This capability expands the scope of scCamAge's utility and also underscores the relevance of studying aging processes across different organisms to uncover common biological principles. scCamAge's ability to provide rapid, high-resolution single-cell age predictions, detailed molecular insights, and cellular morphometric summaries offers a valuable tool for studying aging-related processes in diverse biological contexts.

When we applied the unaltered scCamAge model to human fibroblast senescence datasets with no additional rounds of

learning, we observed significantly superior performance compared to the base InceptionResNet model (vision: v.0.10.0, inception_v3).⁵¹ This indicates that in addition to capturing yeast-specific features associated with the cell wall, scCamAge also identifies other non-peripheral features in human fibroblasts. While recent advancements utilizing cutting-edge AI-based approaches have focused on identifying subcellular compartments undergoing noticeable spatiotemporal changes during senescence induction,^{18–20} these methods primarily capture morphological changes acquired through deep learning, do not consider aging-related bioactivities in predictions, often lack publicly available datasets or final models, and are non-generalized with respect to the model system. scCamAge offers the comprehensive resource of high-quality single-cell image datasets and final prediction models (yeast and human scCamAge) to the community and provides the required toolkit for the holistic understanding of cellular aging and its conserved pathways. In summary, scCamAge represents the first proof of concept in aging research, offering a multi-faceted approach to studying image-based cellular aging dynamics.

Limitations of the study

Despite its robust capabilities, scCamAge has several limitations. First, the yeast scCamAge model was developed solely on CLS datasets, potentially limiting its applicability to RLS assays. However, its framework can be adapted through transfer learning to integrate RLS data. Second, the bioactivity prediction models were tested with a narrow range of extreme drug concentrations, which may not fully reflect aging-induced physiological levels. This limitation can be bypassed by incorporating broader datasets with varied geroprotector concentrations and genetic biosensors such as Rad52-GFP^{52,53} for monitoring DNA damage. Third, the ROIs in chronologically aged yeast cells, often located in the cell wall, may reflect yeast-specific features such as budding activity, limiting their relevance to mammalian cells. Fourth, the drugs and genetic loss-of-function mutants used to validate the scCamAge model are selected for their significant impact on lifespan, ensuring detectable effects. However, these strong effects may also limit the model's ability to accurately detect and measure more subtle changes in longevity. Essentially, while the model can effectively identify major changes due to these interventions, it may not be as sensitive to minor, incremental variations in the aging process. Fifth, while transfer learning has proven valuable in adapting scCamAge from yeast to human datasets, it has inherent limitations. The success of transfer learning relies heavily on the similarity between source and target domains; thus, significant differences in cellular morphology or bioactivities between yeast and human cells may limit its effectiveness. Additionally, the neural network weights trained on yeast chronological aging datasets might not fully capture the complexity of human senescence phenotypes, potentially leading to reduced model sensitivity for subtle features. Sixth, another significant limitation of scCamAge lies in the scarcity of comparable models and datasets for benchmarking. Our literature review identified only a handful of studies utilizing bright-field images for senescent cell prediction and, notably, none addressing chronological aging in yeast. Furthermore, existing human cell-based resources lack openly

accessible models or associated raw data, such as phase-contrast or bright-field images, precluding direct comparisons with scCamAge.^{18–20} Another limitation of scCamAge is the use of YeastSpotter for cell segmentation, which resulted in approximately 28.8% of cells being lost due to imperfect segmentation; this issue could be mitigated by adopting advanced methods such as Cellpose⁵⁴ or StarDist⁵⁵ for improved accuracy. Lastly, only a limited number of aging-associated bioactivities were included, yet these significantly enhanced the model's performance on human datasets. Expanding the repertoire to include markers for telomere length, cell-cycle activity, and autophagy could further strengthen scCamAge's predictive utility across diverse biological systems.

RESOURCE AVAILABILITY

Lead contact

Further information and requests for any additional information that is not provided in the shared resources should be addressed to and will be fulfilled by the lead contact, Gaurav Ahuja (gaurav.ahuja@iitd.ac.in).

Materials availability

This study did not generate new unique reagents.

Data and code availability

The raw RNA-seq files data have been deposited at ArrayExpress under accession E-MTAB-14108 and are publicly available as of the date of publication. Raw metabolomics data files are deposited at MetaboLights under accession ID MTBLS12071 and are publicly available as of the date of publication. Additional information, including datasets, can be accessed using <https://the-ahuja-lab.shinyapps.io/scCamAge/> and are also available on Zenodo via <https://doi.org/10.5281/zenodo.14191724>. The source code, the Docker Image of scCamAge, and the step-by-step user protocol are available at <https://github.com/the-ahuja-lab/scCamAge/> or can be accessed via <https://doi.org/10.5281/zenodo.14545642>. scCamAge is free for academic institutions; however, a commercial license key is mandatory for commercial usage.

ACKNOWLEDGMENTS

The authors thank the IT-HelpDesk team of IIT-Delhi for assisting with the computational resources. We thank all members of the Ahuja lab for their intellectual contributions at various stages of this project. We also thank Vamsi K. Yenamandra for sharing the human fibroblasts. The Ahuja lab is supported by the Ramalingaswami Re-entry Fellowship (BT/HRD/35/02/2006), a re-entry scheme of the Department of Biotechnology, Ministry of Science & Technology, Government of India, as well as an intramural start-up grant and Discovery Track Investigator grant from Indraprastha Institute of Information Technology, Delhi. We sincerely thank the Department of Science and Technology (DST) for sponsoring V.G. as part of their DST Inspire Program and the Council of Scientific and Industrial Research for sponsoring S.D. as part of their fellowship program.

AUTHOR CONTRIBUTIONS

The study was conceived by G.A. Computational analysis workflows were designed by G.A., V.G., and S.D. Statistical guidance was provided by D.S. Microscopy datasets were generated by V.G., S.D., S. Solanki, A. Mittal, S.A., A.S., A.A., A.K.S., and N.K.D. Deep-learning workflows were designed by V.G. and M.G. Experimental data analysis support was provided by V.G., S.D., A.M., S.C., S. Satija, and S.K. Dataset compilation and Python notebooks were coded by V.G., M.G., S.T., R.K.P., and S.K.M. Human cell culture-based experiments were supervised, performed, and analyzed by S.A., J.T., A. Mehta, and G.A. Illustrations were drafted by V.G. and S.D. A. Mittal, G.A., and V.G. wrote the paper. All authors have read and approved the manuscript.

DECLARATION OF INTERESTS

The authors declare that they have no competing interests.

STAR★METHODS

Detailed methods are provided in the online version of this paper and include the following:

- **KEY RESOURCES TABLE**
- **EXPERIMENTAL MODEL AND STUDY PARTICIPANT DETAILS**
 - Human cells and yeast strains
- **METHOD DETAILS**
 - Phase contrast microscopy
 - Fluorescence microscopy
 - Drug treatments
 - Imaging of yeast genetic knock-outs and external drug-treated cells
 - scCamAge framework development
 - Model building and testing
 - Mild thermal stress pulsing (MTSP)
 - Chronological lifespan assay
 - Wheat Germ Agglutinin staining
 - RNA isolation and transcriptomics analysis
 - Metabolomics
 - Integrative omics data analysis
 - Senescence induction in human cells
 - Computational analysis of the scCamAge model on human senescence dataset
- **QUANTIFICATION AND STATISTICAL ANALYSIS**

SUPPLEMENTAL INFORMATION

Supplemental information can be found online at <https://doi.org/10.1016/j.celrep.2025.115270>.

Received: September 4, 2024

Revised: December 10, 2024

Accepted: January 15, 2025

Published: February 6, 2025

REFERENCES

1. Phillip, J.M., Wu, P.-H., Gilkes, D.M., Williams, W., McGovern, S., Daya, J., Chen, J., Aifuwa, I., Lee, J.S.H., Fan, R., et al. (2017). Biophysical and biomolecular determination of cellular age in humans. *Nat. Biomed. Eng.* **1**, 0093. <https://doi.org/10.1038/s41551-017-0093>.
2. Guo, J., Huang, X., Dou, L., Yan, M., Shen, T., Tang, W., and Li, J. (2022). Aging and aging-related diseases: from molecular mechanisms to interventions and treatments. *Signal Transduct. Target. Ther.* **7**, 391.
3. López-Otín, C., Blasco, M.A., Partridge, L., Serrano, M., and Kroemer, G. (2023). Hallmarks of aging: An expanding universe. *Cell* **186**, 243–278.
4. Zhou, W., Dinh, H.Q., Ramjan, Z., Weisenberger, D.J., Nicolet, C.M., Shen, H., Laird, P.W., and Berman, B.P. (2018). DNA methylation loss in late-replicating domains is linked to mitotic cell division. *Nat. Genet.* **50**, 591–602.
5. Endicott, J.L., Nolte, P.A., Shen, H., and Laird, P.W. (2022). Cell division drives DNA methylation loss in late-replicating domains in primary human cells. *Nat. Commun.* **13**, 6659.
6. Le Goallec, A., Diai, S., Collin, S., Prost, J.-B., Vincent, T., and Patel, C.J. (2022). Using deep learning to predict abdominal age from liver and pancreas magnetic resonance images. *Nat. Commun.* **13**, 1979.
7. Zhu, H., Chen, J., Liu, K., Gao, L., Wu, H., Ma, L., Zhou, J., Liu, Z., and Han, J.-D.J. (2023). Human PBMC scRNA-seq-based aging clocks reveal ribosome to inflammation balance as a single-cell aging hallmark and super longevity. *Sci. Adv.* **9**, eabq7599.
8. Doshida, Y., Hashimoto, S., Iwabuchi, S., Takino, Y., Ishiwata, T., Aigaki, T., and Ishigami, A. (2023). Single-cell RNA sequencing to detect age-associated genes that identify senescent cells in the liver of aged mice. *Sci. Rep.* **13**, 14186.
9. Nikopoulou, C., Kleinenkuhn, N., Parekh, S., Sandoval, T., Ziegenhain, C., Schneider, F., Giavalisco, P., Donahue, K.-F., Vesting, A.J., Kirchner, M., et al. (2023). Spatial and single-cell profiling of the metabolome, transcriptome and epigenome of the aging mouse liver. *Nat. Aging* **3**, 1430–1445.
10. McKenna, A., and Gagnon, J.A. (2019). Recording development with single cell dynamic lineage tracing. *Development* **146**, dev169730. <https://doi.org/10.1242/dev.169730>.
11. Wu, S.-H.S., Lee, J.-H., and Koo, B.-K. (2019). Lineage Tracing: Computational Reconstruction Goes Beyond the Limit of Imaging. *Mol. Cells* **42**, 104–112.
12. Chen, C., Liao, Y., and Peng, G. (2022). Connecting past and present: single-cell lineage tracing. *Protein Cell* **13**, 790–807.
13. Hsu, Y.-C. (2015). Theory and Practice of Lineage Tracing. *Stem Cell* **33**, 3197–3204.
14. Wagner, D.E., and Klein, A.M. (2020). Lineage tracing meets single-cell omics: opportunities and challenges. *Nat. Rev. Genet.* **21**, 410–427.
15. Xue, Y., Su, Z., Lin, X., Ho, M.K., and Yu, K.H.O. (2024). Single-cell lineage tracing with endogenous markers. *Biophys. Rev.* **16**, 125–139.
16. Ludwig, L.S., Lareau, C.A., Ulirsch, J.C., Christian, E., Muus, C., Li, L.H., Pelka, K., Ge, W., Oren, Y., Brack, A., et al. (2019). Lineage Tracing in Humans Enabled by Mitochondrial Mutations and Single-Cell Genomics. *Cell* **176**, 1325–1339.e22.
17. Garain, A., Ray, B., Singh, P.K., Ahmadian, A., Senu, N., and Sarkar, R. (2021). GRA_Net: A Deep Learning Model for Classification of Age and Gender From Facial Images. *IEEE Access* **9**, 85672–85689.
18. Heckenbach, I., Mkrtchyan, G.V., Ezra, M.B., Bakula, D., Madsen, J.S., Nielsen, M.H., Oró, D., Osborne, B., Covarrubias, A.J., Iddo, M.L., et al. (2022). Nuclear morphology is a deep learning biomarker of cellular senescence. *Nat. Aging* **2**, 742–755.
19. Kusumoto, D., Seki, T., Sawada, H., Kunitomi, A., Katsuki, T., Kimura, M., Ito, S., Komuro, J., Hashimoto, H., Fukuda, K., and Yuasa, S. (2021). Anti-senescent drug screening by deep learning-based morphology senescence scoring. *Nat. Commun.* **12**, 257.
20. Duran, I., Pombo, J., Sun, B., Gallage, S., Kudo, H., McHugh, D., Bousset, L., Barragan Avila, J.E., Forlano, R., Manousou, P., et al. (2024). Detection of senescence using machine learning algorithms based on nuclear features. *Nat. Commun.* **15**, 1041.
21. Weber, L., Lee, B.S., Imboden, S., Hsieh, C.-J., and Lin, N.Y.C. (2023). Phenotyping senescent mesenchymal stromal cells using AI image translation. *Curr. Res. Biotechnol.* **5**, 100120. <https://doi.org/10.1016/j.cribiot.2023.100120>.
22. Zimmermann, A., Hofer, S., Pendleton, T., Kainz, K., Madeo, F., and Carmona-Gutierrez, D. (2018). Yeast as a tool to identify anti-aging compounds. *FEMS Yeast Res.* **18**, foy020. <https://doi.org/10.1093/femsyr/foy020>.
23. Lu, A.X., Zarin, T., Hsu, I.S., and Moses, A.M. (2019). YeastSpotter: accurate and parameter-free web segmentation for microscopy images of yeast cells. *Bioinformatics* **35**, 4525–4527.
24. Szegedy, C., Ioffe, S., Vanhoucke, V., and Alemi, A. (2017). Inception-v4, Inception-ResNet and the impact of residual connections on learning. In Proceedings of the AAAI Conference on Artificial Intelligence, 31 (AAAI Press), pp. 4278–4284. <https://doi.org/10.1609/aaai.v31i1.11231>.
25. Szegedy, C., Liu, W., Jia, Y., Sermanet, P., Reed, S., Anguelov, D., Erhan, D., Vanhoucke, V., and Rabinovich, A. (2014). Going Deeper with Convolutions. Preprint at arXiv. <https://doi.org/10.48550/arXiv.1409.4842>.
26. Targ, S., Almeida, D., and Lyman, K. (2016). Resnet in Resnet: Generalizing Residual Architectures. Preprint at arXiv. <https://doi.org/10.48550/arXiv.1603.08029>.

27. Simonyan, K., and Zisserman, A. (2014). Very Deep Convolutional Networks for Large-Scale Image Recognition. Preprint at arXiv. <https://doi.org/10.48550/arXiv.1409.1556>.
28. Barardo, D., Thornton, D., Thoppil, H., Walsh, M., Sharifi, S., Ferreira, S., Anžić, A., Fernandes, M., Monteiro, P., Grum, T., et al. (2017). The DrugAge database of aging-related drugs. *Aging Cell* 16, 594–597.
29. He, C., Zhou, C., and Kennedy, B.K. (2018). The yeast replicative aging model. *Biochim. Biophys. Acta, Mol. Basis Dis.* 1864, 2690–2696.
30. de Magalhães, J.P., and Toussaint, O. (2004). GenAge: a genomic and proteomic network map of human ageing. *FEBS Lett.* 571, 243–247.
31. Rattan, S., and Kyriazi, M. (2018). The Science of Hormesis in Health and Longevity (Academic Press).
32. Musa, M., Perić, M., Bou Dib, P., Sobočanec, S., Šarić, A., Lovrić, A., Ruđan, M., Nikolić, A., Milosević, I., Vlahovićek, K., et al. (2018). Heat-induced longevity in budding yeast requires respiratory metabolism and glutathione recycling. *Aging* 10, 2407–2427.
33. Scannapieco, A.C., Sørensen, J.G., Loeschke, V., and Norry, F.M. (2007). Heat-induced hormesis in longevity of two sibling *Drosophila* species. *Bio-gerontology* 8, 315–325.
34. Nielsen, E.R., Eskildsen-Helmond, Y.E.G., and Rattan, S.I.S. (2006). MAP kinases and heat shock-induced hormesis in human fibroblasts during serial passaging in vitro. *Ann. N. Y. Acad. Sci.* 1067, 343–348.
35. Chen, C., and Contreras, R. (2004). The bud scar-based screening system for hunting human genes extending life span. *Ann. N. Y. Acad. Sci.* 1019, 355–359.
36. Şeylan, C., and Tarhan, Ç. (2023). Metformin extends the chronological lifespan of fission yeast by altering energy metabolism and stress resistance capacity. *FEMS Yeast Res.* 23, foad018. <https://doi.org/10.1093/femsyr/foad018>.
37. Tacutu, R., Craig, T., Budovsky, A., Wuttke, D., Lehmann, G., Taranukha, D., Costa, J., Fraifeld, V.E., and de Magalhães, J.P. (2013). Human Ageing Genomic Resources: integrated databases and tools for the biology and genetics of ageing. *Nucleic Acids Res.* 41, D1027–D1033.
38. Bitto, A., Wang, A.M., Bennett, C.F., and Kaeberlein, M. (2015). Biochemical Genetic Pathways that Modulate Aging in Multiple Species. *Cold Spring Harb. Perspect. Med.* 5, a025114. <https://doi.org/10.1101/cshperspect.a025114>.
39. Davies, D.M., van den Handel, K., Bharadwaj, S., and Lengfeld, J. (2022). Cellular enlargement - A new hallmark of aging? *Front. Cell Dev. Biol.* 10, 1036602.
40. Sharma, A., Smith, H.J., Yao, P., and Mair, W.B. (2019). Causal roles of mitochondrial dynamics in longevity and healthy aging. *EMBO Rep.* 20, e48395.
41. Tiku, V., Jain, C., Raz, Y., Nakamura, S., Heestand, B., Liu, W., Späth, M., Suchiman, H.E.D., Müller, R.-U., Slagboom, P.E., et al. (2017). Small nucleoli are a cellular hallmark of longevity. *Nat. Commun.* 8, 16083.
42. Sturm, G., Monzel, A.S., Karan, K.R., Michelson, J., Ware, S.A., Cardenas, A., Lin, J., Brís, C., Santhanam, B., Murphy, M.P., et al. (2022). A multi-omics longitudinal aging dataset in primary human fibroblasts with mitochondrial perturbations. *Sci. Data* 9, 751.
43. Li, Y., Jiang, Y., Paxman, J., O'Laughlin, R., Klepin, S., Zhu, Y., Pillus, L., Tsimring, L.S., Hasty, J., and Hao, N. (2020). A programmable fate decision landscape underlies single-cell aging in yeast. *Science* 369, 325–329.
44. Fehrmann, S., Paoletti, C., Goulev, Y., Ungureanu, A., Aguilaniu, H., and Charvin, G. (2013). Aging yeast cells undergo a sharp entry into senescence unrelated to the loss of mitochondrial membrane potential. *Cell Rep.* 5, 1589–1599.
45. Janssens, G.E., and Veenhoff, L.M. (2016). Evidence for the hallmarks of human aging in replicatively aging yeast. *Microb. Cell* 3, 263–274.
46. Carmona-Gutierrez, D., Eisenberg, T., Büttner, S., Meisinger, C., Kroemer, G., and Madeo, F. (2010). Apoptosis in yeast: triggers, pathways, subroutines. *Cell Death Differ.* 17, 763–773.
47. Li, W., and Vijg, J. (2012). Measuring genome instability in aging - a mini-review. *Gerontology* 58, 129–138.
48. Vijg, J., and Montagna, C. (2017). Genome instability and aging: Cause or effect? *Translational. Transl. Med. Aging* 1, 5–11.
49. Shields, H.J., Traa, A., and Van Raamsdonk, J.M. (2021). Beneficial and Detrimental Effects of Reactive Oxygen Species on Lifespan: A Comprehensive Review of Comparative and Experimental Studies. *Front. Cell Dev. Biol.* 9, 628157.
50. Lima, T., Li, T.Y., Mottis, A., and Auwerx, J. (2022). Pleiotropic effects of mitochondria in aging. *Nat. Aging* 2, 199–213.
51. Szegedy, C., Vanhoucke, V., Ioffe, S., Shlens, J., and Wojna, Z. (2015). Rethinking the Inception Architecture for Computer Vision. [arXiv \[cs.CV\]](https://doi.org/10.48550/arXiv.cs.CV.1512.00567).
52. Styles, E.B., Founk, K.J., Zamparo, L.A., Sing, T.L., Altintas, D., Ribeyre, C., Ribaud, V., Rougemont, J., Mayhew, D., Costanzo, M., et al. (2016). Exploring Quantitative Yeast Phenomics with Single-Cell Analysis of DNA Damage Foci. *Cell Syst.* 3, 264–277.e10.
53. Mattiazzini Usaj, M., Yeung, C.H.L., Friesen, H., Boone, C., and Andrews, B.J. (2021). Single-cell image analysis to explore cell-to-cell heterogeneity in isogenic populations. *Cell Syst.* 12, 608–621.
54. Stringer, C., Wang, T., Michaelos, M., and Pachitariu, M. (2021). Celpose: a generalist algorithm for cellular segmentation. *Nat. Methods* 18, 100–106.
55. Weigert, M., and Schmidt, U. (2022). Nuclei Instance Segmentation and Classification in Histopathology Images with Stardist. In 2022 IEEE International Symposium on Biomedical Imaging Challenges (ISBIC) (IEEE), pp. 1–4.
56. He, K., Gkioxari, G., Dollár, P., and Girshick, R. (2017). Mask R-CNN. Preprint at arXiv. <https://doi.org/10.48550/arXiv.1703.06870>.
57. Culjak, I., Abram, D., Pribanic, T., Dzapo, H., and Cifrek, M. (2012). A brief introduction to OpenCV. In 2012 Proceedings of the 35th International Convention MIPRO (IEEE), pp. 1725–1730.
58. He, K., Zhang, X., Ren, S., and Sun, J. (2015). Deep Residual Learning for Image Recognition. Preprint at arXiv.
59. Robbins, H., and Monroe, S. (1951). A Stochastic Approximation Method. *aoms* 22, 400–407.
60. Ruder, S. (2016). An overview of gradient descent optimization algorithms. Preprint at arXiv.
61. Kingma, D.P., and Ba, J. (2014). Adam: A Method for Stochastic Optimization. Preprint at arXiv.
62. Rifkin, R., and Klautau, A. (2004). In defense of one-vs-all classification. *J. Mach. Learn. Res.* 5, 101–141.
63. Ho, T.K. (1995). Random decision forests. In Proceedings of 3rd International Conference on Document Analysis and Recognition, 1 (IEEE), pp. 278–282.
64. Chi, Z. (2002). MLP classifiers: overtraining and solutions. In Proceedings of ICNN'95 - International Conference on Neural Networks (IEEE). <https://doi.org/10.1109/icnn.1995.488180>.
65. Chen, T., and Guestrin, C. (2016). XGBoost: A Scalable Tree Boosting System. In Proceedings of the 22nd ACM SIGKDD International Conference on Knowledge Discovery and Data Mining KDD '16, B. Krishnapuram, ed. (Association for Computing Machinery), pp. 785–794.
66. Tibshirani, R. (1996). Regression Shrinkage and Selection via the Lasso. *J. R. Stat. Soc. Series B Stat. Methodol.* 58, 267–288.
67. Hoerl, A.E., and Kennard, R.W. (2000). Ridge Regression: Biased Estimation for Nonorthogonal Problems. *Technometrics* 42, 80–86.
68. Schindelin, J., Arganda-Carreras, I., Frise, E., Kaynig, V., Longair, M., Pietzsch, T., Preibisch, S., Rueden, C., Saalfeld, S., Schmid, B., et al. (2012). Fiji: an open-source platform for biological-image analysis. *Nat. Methods* 9, 676–682.
69. Love, M.I., Huber, W., and Anders, S. (2014). Moderated estimation of fold change and dispersion for RNA-seq data with DESeq2. *Genome Biol.* 15, 550.

70. Risso, D., Ngai, J., Speed, T.P., and Dudoit, S. (2014). Normalization of RNA-seq data using factor analysis of control genes or samples. *Nat. Biotechnol.* 32, 896–902.
71. Tarazona, S., Furió-Tarí, P., Turrà, D., Pietro, A.D., Nueda, M.J., Ferrer, A., and Conesa, A. (2015). Data quality aware analysis of differential expression in RNA-seq with NOISeq R/Bioc package. *Nucleic Acids Res.* 43, e140.
72. Bindea, G., Mlecnik, B., Hackl, H., Charoentong, P., Tosolini, M., Kirilovsky, A., Fridman, W.-H., Pagès, F., Trajanoski, Z., and Galon, J. (2009). ClueGO: a Cytoscape plug-in to decipher functionally grouped gene ontology and pathway annotation networks. *Bioinformatics* 25, 1091–1093.
73. Xia, J., Psychogios, N., Young, N., and Wishart, D.S. (2009). MetaboAnalyst: a web server for metabolomic data analysis and interpretation. *Nucleic Acids Res.* 37, W652–W660.
74. Pedregosa, F., Varoquaux, G., Gramfort, A., Michel, V., Thirion, B., Grisel, O., Blondel, M., Prettenhofer, P., Weiss, R., Dubourg, V., et al. (2011). Scikit-learn: Machine Learning in Python. *J. Mach. Learn. Res.* 12, 2825–2830.
75. Hanley, J.A., and McNeil, B.J. (1982). The meaning and use of the area under a receiver operating characteristic (ROC) curve. *Radiology* 143, 29–36.
76. Hanley, J.A., and McNeil, B.J. (1983). A method of comparing the areas under receiver operating characteristic curves derived from the same cases. *Radiology* 148, 839–843.

STAR★METHODS

KEY RESOURCES TABLE

REAGENT or RESOURCE	SOURCE	IDENTIFIER
Chemicals, peptides, and recombinant proteins		
Yeast extract	SRLChem	89463
Peptone	SRLChem	41406
Dextrose	SRLChem	42728
Histidine	SRLChem	42437
Leucine	SRLChem	63007
Methionine	SRLChem	19305
Uracil	SRLChem	23622
Adenine	SRLChem	50300
FM TM 4-64FX	Invitrogen	F34653
H ₂ DCFDA	Invitrogen	D399
Tetramethylrhodamine, Ethyl Ester, Perchlorate (TMRE)	Sigma-Aldrich	87917
MG132	Sigma-Aldrich	M7449
Etoposide	Sigma-Aldrich	E1383
Azacytidine	SRLChem	34476
Metformin	Sigma-Aldrich	PHR1084
Spermine	SRLChem	91710
Spermidine	SRLChem	17030
Propidium Iodide	SRLChem	11195
Wheat Germ Agglutinin	Invitrogen	W11261
TRIzol TM reagent	Ambion Life Technologies	15596026
Zymolyase	Sigma-Aldrich	L2524
Chloroform	Merck	1.07024.2521
Glycogen	SRLChem	49740
Isopropanol	Merck	1.94524.2521
RNase-free water	Invitrogen	AM9938
DNase	Thermo Scientific	EN0521
Ethylenediaminetetraacetic acid solution - EDTA	SRLChem	18240
Methanol	Merck	1.94516.9027
Dulbecco's Modified Eagle Medium (DMEM)	Thermo Scientific	11965092
Fetal Bovine Serum	Thermo Scientific	10437010
Camptothecin	Sigma-Aldrich	C9911
DMSO	Himedia	TC349
Beta Galactosidase assay	SRLChem	52714
Deposited data		
RNA Sequencing Data	ArrayExpress	E-MTAB-14108
Metabolomics	MetaboLights	MTBLS12071
scCamAge Database Server	Shiny R	https://the-ahuja-lab.shinyapps.io/scCamAge
Project GitHub Page	GitHub	https://github.com/the-ahuja-lab/scCamAge
scCamAge Datasets	Zenodo	https://doi.org/10.5281/zenodo.14191724
scCamAge GitHub Zenodo	Zenodo	https://doi.org/10.5281/zenodo.14545642
Experimental models: Cell lines		
<i>Homo sapiens</i> Dermal Fibroblasts	Lonza Bioscience	NHDF-Ad; CC-2511

(Continued on next page)

Continued

REAGENT or RESOURCE	SOURCE	IDENTIFIER
Experimental models: Organisms/strains		
<i>Saccharomyces cerevisiae</i> strain BY4741 (<i>MATa his3Δ1 leu2Δ met15Δ ura3Δ</i>)	gift from Kaustab's lab (Delhi University)	EUROSCAF
<i>S. cerevisiae</i> strain BY4741 <i>msw1Δ</i> (<i>MATa his3Δ1 leu2Δ met15Δ ura3Δ msw1Δ::kanMX</i>)	gift from Martin Graef's lab (MPI Aging)	EUROSCAF
<i>S. cerevisiae</i> strain BY4741 <i>alt2Δ</i> (<i>MATa his3Δ1 leu2Δ met15Δ ura3Δ alt2Δ::kanMX</i>)	gift from Martin Graef's lab (MPI Aging)	EUROSCAF
<i>S. cerevisiae</i> strain BY4741 <i>gsy2Δ</i> (<i>MATa his3Δ1 leu2Δ met15Δ ura3Δ gsy2Δ::kanMX</i>)	gift from Martin Graef's lab (MPI Aging)	EUROSCAF
<i>S. cerevisiae</i> strain BY4741 <i>trx1Δ</i> (<i>MATa his3Δ1 leu2Δ met15Δ ura3Δ trx1Δ::kanMX</i>)	gift from Martin Graef's lab (MPI Aging)	EUROSCAF
<i>S. cerevisiae</i> strain BY4741 <i>sod2Δ</i> (<i>MATa his3Δ1 leu2Δ met15Δ ura3Δ sod2Δ::kanMX</i>)	gift from Martin Graef's lab (MPI Aging)	EUROSCAF
<i>S. cerevisiae</i> strain BY4741 <i>kgd1Δ</i> (<i>MATa his3Δ1 leu2Δ met15Δ ura3Δ kgd1Δ::kanMX</i>)	gift from Martin Graef's lab (MPI Aging)	EUROSCAF
<i>S. cerevisiae</i> strain BY4741 <i>adh2Δ</i> (<i>MATa his3Δ1 leu2Δ met15Δ ura3Δ adh2Δ::kanMX</i>)	gift from Martin Graef's lab (MPI Aging)	EUROSCAF
<i>S. cerevisiae</i> strain BY4741 <i>cys4Δ</i> (<i>MATa his3Δ1 leu2Δ met15Δ ura3Δ cys4Δ::kanMX</i>)	gift from Martin Graef's lab (MPI Aging)	EUROSCAF
<i>S. cerevisiae</i> strain BY4741 <i>gre3Δ</i> (<i>MATa his3Δ1 leu2Δ met15Δ ura3Δ gre3Δ::kanMX</i>)	gift from Martin Graef's lab (MPI Aging)	EUROSCAF
<i>S. cerevisiae</i> strain BY4741 <i>ipt1Δ</i> (<i>MATa his3Δ1 leu2Δ met15Δ ura3Δ ipt1Δ::kanMX</i>)	gift from Martin Graef's lab (MPI Aging)	EUROSCAF
<i>S. cerevisiae</i> strain BY4741 <i>met17Δ</i> (<i>MATa his3Δ1 leu2Δ met15Δ ura3Δ met17Δ::kanMX</i>)	gift from Martin Graef's lab (MPI Aging)	EUROSCAF
<i>S. cerevisiae</i> strain BY4741 <i>met2Δ</i> (<i>MATa his3Δ1 leu2Δ met15Δ ura3Δ met2Δ::kanMX</i>)	gift from Martin Graef's lab (MPI Aging)	EUROSCAF
<i>S. cerevisiae</i> strain BY4741 <i>prs3Δ</i> (<i>MATa his3Δ1 leu2Δ met15Δ ura3Δ prs3Δ::kanMX</i>)	gift from Martin Graef's lab (MPI Aging)	EUROSCAF
<i>S. cerevisiae</i> strain BY4741 <i>pho89Δ</i> (<i>MATa his3Δ1 leu2Δ met15Δ ura3Δ pho89Δ::kanMX</i>)	gift from Martin Graef's lab (MPI Aging)	EUROSCAF
<i>S. cerevisiae</i> strain BY4741 <i>pdx3Δ</i> (<i>MATa his3Δ1 leu2Δ met15Δ ura3Δ pdx3Δ::kanMX</i>)	gift from Martin Graef's lab (MPI Aging)	EUROSCAF
Software and algorithms		
OpenCV	4.6.0.66	https://opencv.org/
YeastSpotter	Default GitHub version	http://yeastspotter.csb.utoronto.ca/
MaskR-CNN	Keras == 2.2.4, TensorFlow == 1.10	https://github.com/matterport/Mask_RCNN
scikit-learn	1.3.0	https://scikit-learn.org/stable/

(Continued on next page)

Continued

REAGENT or RESOURCE	SOURCE	IDENTIFIER
XGBoost library	1.7.5	https://pypi.org/project/xgboost/
ClueGo	2.5.10	https://apps.cytoscape.org/apps/cluego
NOISeq	2.48.0	https://www.bioconductor.org/packages/release/bioc/html/NOISeq.html
RUVSeq	1.38.0	https://www.bioconductor.org/packages/release/bioc/html/RUVSeq.html
MetaboAnalyst	6.0	https://www.metaboanalyst.ca/
ImageJ	1.54	https://imagej.net/ij/
Past 4	4.10	https://www.nhm.uio.no/english/research/resources/past/
R	4.4.1	https://www.r-project.org/
RStudio	2024.4.2.764	https://posit.co/download/rstudio-desktop/
Jupyter Notebook	6.5.2	https://jupyter.org/
Python 3	3.9.16	https://www.python.org/
uDocker	1.3.16	https://indigo-dc.github.io/udocker/
Docker	27.1.1	https://www.docker.com/
Other		
Breathe-easy membranes	Sigma-Aldrich	Z380059
Fluorescence and Phase contrast Microscope	Nikon	Eclipse Ci-L
Camera	Nikon	DS-Qi2 camera
Bioteck Synergy HTX multi-mode reader	Bioteck	HTX multi-mode reader
1290 Infinity HPLC	Agilent Technologies, Santa Clara, CA, USA	
6545 QTOF	Agilent Technologies, Santa Clara, CA, USA	
Brightfield Microscope	Creuzet	Tissue Culture Trinocular

EXPERIMENTAL MODEL AND STUDY PARTICIPANT DETAILS

Human cells and yeast strains

All the model-building and iterative thermal pulsing experiments were performed on the *Saccharomyces cerevisiae* strain BY4741 (*MATa his3Δ leu2Δ0 met15Δ ura3Δ*). For the validation purpose, we have used yeast genetic knockouts of *msw1Δ*, *alt2Δ*, *gsy2Δ*, *trx1Δ*, *sod2Δ*, *kgd1Δ*, *adh2Δ*, *cys4Δ*, *gre3Δ*, *ipt1Δ*, *met17Δ*, *met2Δ*, *prs3Δ*, *pho89Δ* and *pdx3Δ* genes on the background strain of BY4741 (*MATa xxx::kanMX his3Δ leu2Δ ura3Δ0 met15Δ*). Yeast cells were cultured in yeast extract–peptone–dextrose (YPD) medium (1% yeast extract, 2% peptone, and 2% dextrose) and Synthetic Complete (SC) Media (2% glucose, 20 mg/L histidine, 120 mg/L leucine, 20 mg/L methionine, 20 mg/L uracil, and 20 mg/L adenine) at 30°C and 150 rpm.

METHOD DETAILS

Phase contrast microscopy

To generate models and validation datasets, the yeast primary culture was grown in a YPD medium at 30°C for 18 h. Following this, a secondary culture was set up using the primary culture under consistent environmental parameters. For subsequent experiments, 10 µL of the secondary culture was inoculated into Deep-well plates containing 1 mL of SC medium, with the plates subsequently sealed using breathe-easy membranes (Z380059, Sigma-Aldrich). Sampling for microscopic imaging was conducted on alternative days from day 2 to day 20. Cellular samples were concentrated via centrifugation, and 5 µL of the concentrated sample was placed onto microscope slides for imaging. Microscopic images were acquired utilizing a Nikon Eclipse Ci-L Fluorescence Microscope outfitted with a phase contrast filter. Imaging was performed at a magnification of 100×, with an exposure period of 10 ms.

Fluorescence microscopy

Wild-type (WT) yeast cells were cultured in SC media using the previously established methodology. 100 µL aliquots were extracted every two days from five biological replicates to monitor cellular responses. Subsequently, cells were pelleted down at 6000 rpm for

3 min, and the cell pellet was resuspended in 100 μ L of fresh 1X phosphate-buffered saline (PBS) supplemented with the respective working concentrations of fluorescent dyes: FM 4-64FX (F34653, Invitrogen) at 5 μ M, H₂DCFDA (D399, Invitrogen) at 10 μ M, and TMRE (87917, Sigma) at 25 nM. Following the dye treatment, the cells were incubated in the dark at 30°C for 30 min to ensure dye uptake and labeling. After incubation, cells were washed and resuspended in fresh 1X PBS to remove excess dye. Subsequently, 5 μ L samples from each condition were collected and subjected to microscopic examination using a Nikon Eclipse Ci-L Fluorescence Microscope. For imaging of TMRE-labeled cells (TRITC filter), an exposure time of 100 ms was used. H₂DCFDA (FITC filter) and FM 4-64FX (TRITC filter) were imaged with a 2 s exposure period to capture fluorescence signals.

Drug treatments

WT yeast cells were grown until secondary culture and were transferred to the SC medium after completion, and different concentrations of MG132 (M7449, Sigma), etoposide (E1383, Sigma), and azacytidine (34476, SRL) were added to the cells. The cells were treated for 4 h with azacytidine (10 mM and 30 mM), 1 h with etoposide (1 μ M and 25 μ M), and 2 h with MG132 (25 μ M and 100 μ M), respectively. After incubation, phase contrast microscopic images of cells were taken at 100X resolution using the Nikon Eclipse Ci-L Fluorescence Microscope at 10 ms exposure time.

Imaging of yeast genetic knock-outs and external drug-treated cells

To validate the scCamAge model's efficacy, we used yeast genetics knockouts (KOs), which were cultured as mentioned above. Nine pro-longevity and six anti-longevity phenotypic yeast genetic KOs were chosen, and microscopic images were taken every other day (day 2 to day 20).³⁰ Also, to check if scCamAge will be able to capture the pro-longevity effect of known pro-longevity drugs, metformin (PHR1084, Sigma) (working concentration 50 mM), spermine (91710, SRL) (working concentration 1 mM), and spermidine (17030, SRL) (working concentration 1 mM) were treated to the cells in the drug-treated condition and microscopic images were taken on every other day (day 2-day 20).

scCamAge framework development

The construction of scCamAge involves building a dataset using phase-contrast images of yeast cells that were collected from Day 2 to Day 20 (explained above). To identify each of the yeast cells in micrographs, we have used *yeastspotter*,²³ a method that uses the Mask Region-based Convolutional Neural Network (MaskR-CNN model) for segmentation. MaskR-CNN is an extended version of Faster R-CNN that is used for segmentation tasks, like identifying items in an image and accurately drawing their borders. Various essential components make up the Mask R-CNN approach. Firstly, it extracts information from the input image using a backbone convolutional neural network (CNN); then, these features are fed two simultaneous subnetworks, one for object identification and the other for producing segmentation masks.⁵⁶ Once the masked image was generated, the contours image, i.e., single yeast micrographs, were extracted using thresholding methods along with the masked images. To calculate the area as well as the perimeter of the micrographs, OpenCV (Open Source Computer Vision Library) functions (*cv2.contourArea()*, *cv2.contourArea()*) were used.⁵⁷ After extracting all the single yeast micrographs, model building was done to create scCamAge.

To build robust scCamAge, we used multiple transfer learning models and chose the best model to predict the age of yeast cells. Four main models were tested in order to get a robust scCamAge model. VGG19 is an extension to VGG16, which pushes the depth from 16 to 19 layers in the deep convolutional neural network; here, layers represent the weighted or convolutional layers, hence the name VGG19. VGG19 takes a 224 \times 224 image size and utilizes small 3 \times 3 convolutional filters that capture the information from left/right and up/down.²⁷ ResNet50 is a robust convolutional neural network with 50 layers, including 48 convolutional layers, one MaxPool layer, and one average pool layer. One main feature is skip connection, which allows information from earlier layers to be preserved, which aids in better representation of input data by adding the output of an earlier layer to a later layer.⁵⁸ GoogLeNet (vision:v0.10.0, googlenet), known as Inception Network, was developed by Google researchers. The network is 22 layers deep and, hence, computationally less expensive. It uses an inception module with multiple parallel branches with different convolutional filters (1x1, 3x3, 5x5) and a max-pooling layer. The output of these branches is connected to the next layer. It contains two auxiliary classifiers connected to the outputs of Inception (4a) and Inception (4d). These classifiers are used during training to improve model performance. Ultimately, it has global average pooling that helps combat the gradient vanishing problem and reduces the number of trainable parameters.²⁵ Finally, the selected model was InceptionResNet (vision:v0.10.0, inception_v3), a convolutional neural network architecture that was improved in several ways over its predecessors. Its high accuracy is well-known and intended for micrograph categorization jobs. It has label smoothing, a regularization technique that helps overfit the models by smoothing the labels during training, reducing the confidence of the model's predictions. It has a factorized 7 \times 7 convolution, which is broken into two 3 \times 3 convolutions that improve computational efficiency. To enhance convergence and lessen the vanishing gradient issue in deep networks, the auxiliary classifier is employed to propagate label information lower down the network. It uses batch normalization in the sidehead of the network, which improves the stability and convergence of the model during training.⁵¹

The robustness of the final model was ensured through extensive hyperparameter tuning. The dataset was divided into a train-validation-test split of 70%, 10%, and 20%, respectively. The model was trained for 150 epochs during the tuning process to identify the optimal learning rate and the most effective optimization method (Table S7). For hyperparameter tuning, we experimented with learning rates of 0.01, 0.001, and 0.0001, as well as batch sizes of 32 and 64. The final hyperparameter settings were selected based on their ability to maximize model performance and generalizability, ensuring a robust and reliable model. Two optimization

algorithms were used to get the best fit for the dataset. SGD (Stochastic Gradient Descent)^{59,60} is used in deep learning, and it updates the network parameters based on the gradients of the loss function with respect to the parameters. Adam Optimizer is a modification of SGD that uses the moving average of the first and second moments of the gradients to adapt the learning rates for each parameter.⁶¹

Model building and testing

The data was split into training data (80%) and testing data (20%) to build models. Each model underwent hyperparameter tuning, and the best-performing model was selected. To ensure robustness, 10-fold cross-validation was performed on the finally selected hyperparameters. In order to evaluate the AUC-ROC of the scCamAge model, the One-vs.-All (OvA) method was used. This approach involves training a binary classifier, where one class is positive, and the rest of the classes are considered negative for each class. Next, we compute the AUC ROC curve for every binary classifier. The overall AUC ROC curve for the multi-class model is produced by averaging the AUC ROC curves of each binary classifier.⁶²

The features were extracted from the scCamAge model to create the regression and classification models. The same split was used for training and testing data (80-20%) and multiple models such as random forest, which is a supervised learning method and bagging technique that uses ensemble learning for regression models,⁶³ Multi-Layer Perceptron (MLP) Regressor: a neural network that consists of multiple layers of the node which are connected to subsequent nodes,⁶⁴ XGBRegressor; a part of XGBoost library and are efficient and scalable,⁶⁵ Least Absolute Shrinkage and Selection Operator (LASSO) a statistical method that combines variable selection and regularization and increases the accuracy and final chosen model.⁶⁶ Ridge regression is a regularization technique that addresses multicollinearity and overfitting by adding the penalty in the cost function. It is more effective in datasets that have high correlation. The main strength of the penalty term is controlled by hyperparameter λ , where if λ increases, there will be more shrinkage of the coefficients and hence less overfitting. It is best suited in computational biology, genetics, and environmental studies, where data is multicollinear. A similar approach was used for the classification model, i.e., random forest, Multi-Layer Perceptron (MLP), support vector machine (SVM), Gaussian Naive Bayes (GNB), Gradient Boosting Classifier (GBC), Stochastic Gradient Descent (SGD), Logistic Regression (LR), and Extra Tree Classifier (ET).⁶⁷ The final model was selected based on the parameters' performances and was checked for robustness using 10-fold cross-validation (CV).

Mild thermal stress pulsing (MTSP)

The WT yeast strain was inoculated in a YPD medium for the primary culture and maintained at 30°C for 18 h. Cells were divided into three groups for three different thermal pulsing conditions. In the first condition, cells were maintained at 30°C for 15 min, followed by another 15 min at 37°C, resulting in a single cycle of thermal pulsing (TP). In the second condition, a steady state (SS) was created when the cells were kept at 30°C for both of the 15-min time intervals. In the third condition, cells were maintained at 37°C for the two 15-min intervals, creating a heat shock (HS) scenario. In the first stage, the cells were pulsed for ten cycles under each of the three conditions, and the pulsed cells were used to set up the primary culture. Heat pulsing was applied to the cells for an additional fifteen cycles after the primary culture was finished using the previously mentioned methods. Following 25 cycles, thermal pulsing cells were moved to a deep-well plate containing SC media, and micrographs were obtained using the aforementioned phase contrast microscopy methodology.

Chronological lifespan assay

Pulsed cells from 25 cycles (13 μ L) were added as an inoculant to deep-well plates containing 1.3 mL of SC medium, and the plates were covered with a Breathe-Easy membrane (Z380059, Sigma). A cell aliquot was used for the propidium iodide-based cell viability quantification experiment on Days 1, 3, 5, 10, 15, and 20. During the aforementioned days, a 50 μ L aliquot was combined with 50 μ L of newly made Propidium Iodide (PI; 11195, SRL) staining solution in 1x PBS to achieve a final PI concentration of 5 μ g/mL in 96-well black plates, which were incubated for 20-min in dark. The positive control in this experiment was heat-killed (HK) cells. A Bioktek Synergy HTX multi-mode reader was used to measure the fluorescence at 530/25 nm and 590/25 nm, respectively, for excitation and emission wavelengths. OD600 was measured using a further 50 μ L aliquot from the same plates following a 1:2 dilution with 1X PBS. The fluorescence measurements were first normalized in the data analysis using the corresponding well's blank normalized OD600 values. After that, the normalization process was carried out using heat-killed cells, which were adjusted at 100% death. To prevent negative percentages, the percent death was set at 100% if a sample exhibited higher fluorescence than the HK cell. These data were deducted from 100% to calculate the survival percentage, and any outliers were eliminated. The survival statistics for each day were then normalized to the experiment's first day, which was set at 100% survival.

Wheat Germ Agglutinin staining

Initially, cells were treated with 25 cycles of thermal pulsing. After that, 10 μ L of the cell was used to establish a 1 mL culture in the deep-well plate at SC medium and maintained at 30°C. On day 5, a 100 μ L cell aliquot was taken from five different biological replicates. The cells were resuspended in 100 μ L of fresh 1X PBS. Then, cells were treated with Wheat Germ Agglutinin (WGA; InvitrogenTM, W11261) (final concentration of 1 μ g/mL) and kept in the dark for 45 min at 30°C. Following incubation, the cells were pelleted down at 6000 rpm for 3 min, and the pellet was resuspended in 15 μ L of fresh 1X PBS. From this, 5 μ L was used for microscopy (Nikon Eclipse Ci-L Fluorescence Microscope with a Nikon DS-Qi2 camera) using a FITC filter for green fluorescence.

The images were obtained with an exposure time of 600 ms. Images were opened on ImageJ,⁶⁸ and each green dot was counted manually for the analysis.

RNA isolation and transcriptomics analysis

Using the aforementioned methods in Mild Thermal Stress Pulsing (MTSP) cells, twenty-five-cycle pulsed cells were produced and pelleted down. Then, cells were treated with zymolyase (40 units) and mechanically broken down with glass beads. After centrifuging the lysed cell suspension into fresh MCT, 500 µL of TRIzol reagent (15596026, Ambion Life Technologies) was used to dissolve the pellet. 500 µL of cold chloroform was added and kept for 15 min for mechanical breakdown and, after completion, incubated for another 5 min at room temperature; after that, it was centrifuged at 12000 g for 15 min at 4°C. A fresh MCT with 250 µL of chilled isopropanol was added with the upper aqueous layer, which was gently transferred, and an additional 1 µL of glycogen was added to accelerate the RNA precipitation, followed by a 30-min incubation at -80°C. Centrifugation at 12,000 g for 15 min at 4°C was used to pellet down nucleic acid. The pellet was air dried after being cleaned with 70% ethanol at 5000 g for 5 min at 4°C. It was then re-suspended in RNase-free water. To eliminate DNA contamination, samples were processed with DNase for 15 min at 37°C. DNase was inactivated using 5 mM EDTA and 10 min of heat at 65°C. This pure RNA was again resuspended in RNase-free water for further processing.

RUVSeq, a method based on a widely used approach for normalization, was used to analyze the transcriptomics data to remove unwanted variation from RNA-Seq data. DESeq2 was also used for differential analysis of count data; it enhances the stability and interpretability of results by utilizing fold changes and shrinkage estimation for dispersions. This makes it possible to do a more quantitative study concentrating on the degree of differential expression instead of its mere existence. We also used NOISeq, which considers both technical and biological replicates. It comprises a statistical framework for RNA-seq Differential Enrichment analysis that evaluates variations in gene expression between conditions by constructing an empirical distribution instead of depending on parametric assumptions.^{69–71} Once we got the differential genes, we used the ClueGo tool, which connects the genes to the pathways.⁷²

Metabolomics

WT yeast cells were pulsed for 40 cycles as per the Mild Thermal Stress Pulsing (MTSP) methodology. Once finished, cells were moved to a micro-centrifuge-tube and centrifuged at 6000 rpm for 5 min at room temperature to pellet down the cells. After adding zymolyase enzyme (L2524, Sigma-Aldrich) to the cell pellet at a final 40 units/mL concentration in 1X PBS, the mixture was incubated for 1 h at 30°C. After that, the cells were washed with 1X PBS, and the cell pellet was kept at -80°C until metabolomics was performed.

Metabolomics was carried out using a 1290 Infinity HPLC and a 6545 QTOF (Agilent Technologies, Santa Clara, CA, USA) with two ESI sources. Jasmonic acid, Gibberellic acid, zeatin, Tryptophan 15N, Estrone D4, Arginine 15N, Thiamine D4, 15N5-8-OH-2-dG, 13C12 dityrosine, and 8-PGF2-D4 are some of the internal controls utilized in metabolomics. The protein precipitation procedure was applied to prepare the sample. In summary, 10 µL of a cocktail, including internal standards for commercial stable isotopes, was added, and then 750 µL of cold methanol: water (4:1) was added, and the probe was sonicated. Subsequently, 450 µL of cooled chloroform was added and vortexed for 5 min. Next, 150 µL of chilled water was added, vortexed for 30 min, and the sample was stored at -20°C. For the separation of the methanol and chloroform layers, samples were centrifuged for 10 min at 5000 rpm and 4°C. The two layers were gathered, vacuum-concentrated, dried at 30°C, and then reconstituted in 100 µL of methanol: water (1:1). To monitor instrument drift and assess signal reproducibility, Quality Control (QC) samples were injected every five samples. According to Pearson's rank order, there was a substantial correlation ($r > 0.9$) between the QCs ($n = 6$), indicating that differences were not statistically significant. Untargeted metabolomics data analysis was performed using MetaboAnalyst (<https://www.metaboanalyst.ca/>).⁷³

Integrative omics data analysis

Integrative omics data analysis was done with the help of MetaboAnalyst software (explained above). Integrative omics analysis is done using transcriptomics and metabolomics data. In this analysis, the genes that are differentially enriched in the transcriptomic data and the differentially abundant metabolites are used to identify the essential pathways involved in the study's mechanism.⁷³

Senescence induction in human cells

Human dermal fibroblasts (NHDF-Ad; CC-2511, Lonza Bioscience) were used for the senescence assay. Briefly, cells were cultivated in a T-75 flask with 10% Fetal Bovine Serum (FBS)-Dulbecco's Modified Eagle Medium (DMEM). Upon reaching 70% confluence, the cells were split and seeded onto coverslips in 6-well plates with approximately 1500 cells in each well. The cells were incubated in a CO₂ incubator till the cells reached a confluence of about 30% (~2 days). Subsequently, the cells were treated with camptothecin (CPT) for senescence induction, as suggested by Kusumoto et al.¹⁹ Notably, we used a concentration gradient of 6.25 nM, 12.5 nM, 25 nM, 50 nM, and 100 nM for senescence induction. Additionally, we also used solvent control (DMSO) and untreated cells as controls for this assay and incubated the cells for 48 h in a CO₂ incubator.

Notably, we tested CPT potency in inducing senescence across these tested concentrations using Senescence Associated Beta Galactosidase assay (SA-βgal assay), and image acquisition was performed using Creuzet Tissue Culture Trinocular Microscope at 5X magnification. Quantification of the senescence of positive and negative cells was then performed using ImageJ

software (<https://imagej.net/software/fiji>).⁶⁸ Furthermore, for preparing the CPT dataset, the coverslips from each well were inverted onto DPX mountant on a slide to capture the phase contrast images of human dermal fibroblast cells. Notably, imaging was performed at 10X magnification using a Nikon Eclipse Ci-L fluorescence microscope with an exposure time of 3 ms and analog gain of 64X.

Computational analysis of the scCamAge model on human senescence dataset

To test the applicability of the scCamAge model in predicting human senescence cells, we tested this on two independent datasets: first, the in-house created camptothecin-induced senescence of human fibroblast cells, and second, we utilized a publicly available dataset of replicative senescence of human fibroblasts.⁴² We compared the image features extracted from scCamAge, features from the bioactivity prediction module of scCamAge, combined features of image and bioactivity, and generic InceptionResNet image features. We used a Random Forest classifier and performed 10-fold cross-validation in this comparison. We also performed the One-vs.-All analysis on all the test predictions of each fold. Model and evaluation were done using sci-kit-learn packages.⁷⁴

QUANTIFICATION AND STATISTICAL ANALYSIS

All statistical analyses were performed using the statistical packages provided within the R programming framework. A two-sided Mann-Whitney U test was used to compare the medians of the two distributions (non-parametric). Student's t-test was used to compare the mean of the two groups. Analysis of covariance (ANCOVA) was used, which accounts for the effect of continuous variables that co-vary with the dependent. ANCOVA was used to examine the main effects of categorical factors and their interaction on a continuous dependent variable. The One-vs.-All AUC scores method by Hanley & McNeil was used to compare the One-vs.-All AUC scores.^{75,76} The p-value cutoff used in this study is 0.05. *, **, ***, and **** refer to p-values <0.05, <0.01, <0.001, and <0.0001, respectively.